Monthly Notices of the ROYAL ASTRONOMICAL SOCIETY

MNRAS **546,** 1–24 (2026) https://doi.org/10.1093/mnras/stag115
Advance Access publication 2026 January 19

BlackTHUNDER: Shedding light on a dormant and extreme little red dot at $z = 8.50$

Gareth C. Jones [1,2]★ Hannah Übler [3] Roberto Maiolino [1,2,4] Xihan Ji [1,2] Alessandro Marconi [5,6] Francesco D'Eugenio [1,2] Santiago Arribas [7] Andrew J. Bunker [8] Stefano Carniani [9] Stéphane Charlot [10] Giovanni Cresci [11] Kohei Inayoshi [12] Yuki Isobe [1,2] Ignas Juodžbalis [1,2] Giovanni Mazzolari [3,13] Pablo G. Pérez-González [7] Michele Perna [7] Raffaella Schneider [14] Jan Scholtz [1,2] and Sandro Tacchella [1,2]

[1]*Kavli Institute for Cosmology, University of Cambridge, Madingley Road, Cambridge CB3 0HA, UK*
[2]*Cavendish Laboratory, University of Cambridge, 19 JJ Thomson Avenue, Cambridge CB3 0HE, UK*
[3]*Max-Planck-Institut für extraterrestrische Physik, Gießenbachstraße 1, D-85748 Garching, Germany*
[4]*Department of Physics and Astronomy, University College London, Gower Street, London WC1E 6BT, UK*
[5]*Dipartimento di Fisica e Astronomia, Università degli Studi di Firenze, Via G. Sansone 1, I-50019, Sesto Fiorentino, Firenze, Italy*
[6]*INAF – Osservatorio Astrofisico di Arcetri, Largo E. Fermi 5, I-50125, Firenze, Italy*
[7]*Centro de Astrobiología (CAB), CSIC-INTA, Ctra. de Ajalvir km 4, Torrejón de Ardoz, E-28850, Madrid, Spain*
[8]*Department of Physics, University of Oxford, Denys Wilkinson Building, Keble Road, Oxford OX1 3RH, UK*
[9]*Scuola Normale Superiore, Piazza dei Cavalieri 7, I-56126 Pisa, Italy*
[10]*Institut d'Astrophysique de Paris, Sorbonne Université, CNRS, UMR 7095, 98 bis bd Arago, F-75014 Paris, France*
[11]*INAF – Osservatorio Astrofisco di Arcetri, largo E. Fermi 5, I-50127 Firenze, Italy*
[12]*Kavli Institute for Astronomy and Astrophysics, Peking University, Beijing 100871, China*
[13]*INAF – Osservatorio di Astrofisica e Scienza dello Spazio di Bologna, Via Gobetti 93/3, I-40129 Bologna, Italy*
[14]*Dipartimento di Fisica, Sapienza Universitá di Roma, Piazzale Aldo Moro 5, I-00185 Rome, Italy*

Accepted 2026 January 12. Received 2025 December 18; in original form 2025 September 24

ABSTRACT

Recent photometric surveys with *James Webb Space Telescope (JWST)* have revealed a significant population of mysterious objects with red colours, compact morphologies, frequent signs of active galactic nucleus (AGN) activity, and negligible X-ray emission. These 'little red dots' (LRDs) have been explored through spectral and photometric studies, but their nature is still under debate. As part of the BlackTHUNDER survey, we have observed UNCOVER_20466, one of the most distant LRDs known ($z = 8.5$), with the *JWST*/NIRSpec Integral Field Unit (IFU). Previous *JWST*/NIRCam and *JWST*/NIRSpec MSA observations of this source revealed its LRD nature, as well as the presence of an AGN. Using our NIRSpec IFU data, we confirm that UNCOVER_20466 is an LRD (based on spectral slopes and compactness) that contains an overmassive black hole. However, our observed Balmer decrements do not suggest strong dust attenuation, resulting in a lower H β-based bolometric luminosity and $\lambda_{\rm Edd}$ (~ 10 per cent) than previously found. This source lies on local relations between $M_{\rm BH} - \sigma_*$ and $M_{\rm BH} - M_{\rm dyn}$, suggesting that this could be a progenitor of the core of a lower-redshift galaxy. We explore the possible evolution of this source, finding evidence for substantial black hole accretion in the past and a likely origin as a heavy seed at high redshift ($\sim 10^3\,{\rm M}_\odot$). Ly α emission is strongly detected, implying $f_{\rm esc}^{{\rm Ly}\,\alpha} \sim 30$ per cent. The extremely high [O III]λ4363/H γ ratio is indicative of not only AGN photoionization and heating, but also extremely high densities ($n_{\rm e} \sim 10^7\,{\rm cm}^{-3}$), suggesting that this black hole at such high redshift may be forming in an ultra-dense protogalaxy.

Key words: galaxies: active – galaxies: high-redshift – quasars: supermassive black holes.

1 INTRODUCTION

The advent of *James Webb Space Telescope* (*JWST*) has revolutionized the field of high-redshift galaxy evolution, including the spectroscopic confirmation of galaxies at $z > 10$ (within the first ~ 500 Myr of the Universe; e.g. E. Curtis-Lake et al. 2023; S. Carniani et al. 2024; R. P. Naidu et al. 2025b), the construction of ultraviolet (UV) luminosity functions out to high redshift from photometric candidates (e.g. C. T. Donnan et al. 2024; B. Robertson et al. 2024; L. Whitler et al. 2025b), and new constraints on the progression and topology of ionization of the Universe by galaxies in the epoch of reionization (e.g. R. Endsley et al. 2024; C. Simmonds et al. 2024; L. Whitler et al. 2025a). One of the more

★ E-mail: gj283@cam.ac.uk

surprising findings was the discovery of numerous compact, red objects in *JWST*/NIRCam data, which were given the name 'little red dots' (LRDs; J. Matthee et al. 2024). While a few red, compact sources were found to be local brown dwarfs (D. Langeroodi & J. Hjorth 2023; K. N. Hainline et al. 2024), LRDs are primarily high-redshift galaxies (i.e. peaking in number between $4.5 < z < 8.0$; e.g. D. D. Kocevski et al. 2025).

The red nature of these galaxies is usually caused by a distinctive 'v'-shaped continuum from rest-optical to rest-UV, which is caused by red UV slopes ($\beta_{\rm UV} \sim -1.5$; compared to the bluer $\beta_{\rm UV} \sim -2.4$ found for star-forming galaxies; e.g. A. Saxena et al. 2024a; M. W. Topping et al. 2024b; D. Dottorini et al. 2025) and positive optical slopes ($\alpha_{\rm opt} > 0$ where slopes are defined as $F_\lambda \propto \lambda^{\beta_{\rm UV}||\alpha_{\rm opt}}$; e.g. J. E. Greene et al. 2024). Their compactness is usually defined as a ratio of *JWST*/NIRCam photometric fluxes within different apertures (e.g. $C_{444W} \equiv f_{444}(0.4'')/f_{444}(0.2'') \lesssim 1.7$; V. Kokorev et al. 2024; H. B. Akins et al. 2025b; I. Labbe et al. 2025). In addition, many photometrically selected LRDs show broad hydrogen Balmer emission lines without similar broad emission in forbidden oxygen lines, which is robust evidence for an AGN nature (e.g. L. J. Furtak et al. 2023b; J. E. Greene et al. 2024; J. Matthee et al. 2024; R. E. Hviding et al. 2025; D. D. Kocevski et al. 2025). But unlike other AGN candidates, most LRDs are undetected in X-ray (e.g. T. T. Ananna et al. 2024; G. Mazzolari et al. 2024; M. Yue et al. 2024; R. Maiolino et al. 2025b; A. Sacchi & Á. Bogdán 2025) or submm/radio observations (e.g. C. M. Casey et al. 2025; G. Mazzolari et al. 2025; E. A. Orozco et al. 2025; D. J. Setton et al. 2025a; M. Xiao et al. 2025; but cf. S. Fu et al. 2025; M. Golubchik et al. 2025; L. F. Rodriguez & I. F. Mirabel 2025).

The nature of these sources is still under debate, as their properties are not trivially explained by common galactic models. This ambiguity is partially due to the fact that their natures can be described either by active galactic nucleus (AGN)-dominated galaxies or compact, dusty, star-forming galaxies (e.g. J. F. W. Baggen et al. 2024). Some investigations have looked into this by using different spectral energy distribution (SED) models: galaxy-only, AGN-only, and a combination of an AGN and host galaxy (hybrid; e.g. V. Kokorev et al. 2023; R. Tripodi et al. 2024; G. C. K. Leung et al. 2025; K. Ronayne et al. 2025). While these models can all fit the observed photometry of LRDs, it is difficult to robustly constrain the contribution of the AGN to the photometry of these sources. Therefore, the hybrid models return significantly lower stellar mass and dust attenuation ($A_{\rm V}$; e.g. M. Carranza-Escudero et al. 2025), but with high uncertainty on both physical quantities.

Previous works have suggested that LRDs represent black holes (either single or binary systems) embedded in massive gaseous envelopes (e.g. K. Inayoshi et al. 2025; X. Ji et al. 2025b; D. Kido et al. 2025; X. Lin et al. 2025; R. P. Naidu et al. 2025b; M. C. Begelman & J. Dexter 2026), possibly in the earliest phase of accretion (K. Inayoshi 2025; R. Maiolino et al. 2025a), while others explore whether their properties could be explained by self-interacting dark matter haloes (e.g. W.-X. Feng, H.-B. Yu & Y.-M. Zhong 2025; M. G. Roberts et al. 2025), super-Eddington accretion (e.g. H. Liu et al. 2025), or population III supermassive stars (e.g. D. Nandal & A. Loeb 2025; C. Jockel et al. 2026).

Among the most extreme LRDs is the source UNCOVER_20466 ($\alpha = 3.640409$, $\delta = -30.386437$, $z = 8.50$), which was observed with *JWST*/NIRCam as part the *JWST* Cycle 1 Treasury programme UNCOVER ('Ultra-deep NIRCam and NIRSpec Observations Before the Epoch of Reionization'; PID 2561; PIs: I. Labbe, R. Bezanson; R. Bezanson et al. 2024). I. Labbe et al. (2025) searched these data for objects with red colours (based on F115W to F444W colours) and compact morphology ($f_{\rm F444W}(r < 0.2\,{\rm arcsec})/f_{\rm F444W}(r < 0.1\,{\rm arcsec}) < 1.7$) that were well-detected in F444W (S/N > 14). This resulted in a sample of 26 reddened AGN candidates out of a parent sample of 5×10^4 sources. UNCOVER_20466 was included as an AGN candidate[1] with a very compact morphology ($r_{\rm e} = 0.026$ arcsec) indistinguishable from the point spread function (PSF). Although UNCOVER_20466 is gravitationally lensed by the Abell 2744 galaxy cluster, L. J. Furtak et al. (2023a) find that UNCOVER_20466 is only gravitationally magnified by a factor $\mu = 1.33^{+0.01}_{-0.02}$. The best-fitting photometric redshift was quite low ($z_{\rm phot} = 5.17$), resulting in skewed best-fitting parametres (e.g. $M_{\rm UV}$, M_*). The properties of UNCOVER_20466 appeared to qualify it for the classification of an LRD, and D. Langeroodi & J. Hjorth (2023) confirmed that the LRD nature of UNCOVER_20466 represents an extragalactic object rather than a brown dwarf.

UNCOVER_20466 was then observed with the *JWST*/NIRSpec MSA, using the PRISM/CLEAR disperser/filter combination (spectral resolving power $R \sim 100$) and an exposure time of 2.7 h. By analysing the resulting spectrum, V. Kokorev et al. (2023) found a higher spectroscopic redshift ($z_{\rm spec} = 8.50$, resulting in $M_{\rm UV} = -18.11$; S. Fujimoto et al. 2024) and strong evidence for the presence of a broad-line AGN (see also analysis of J. E. Greene et al. 2024). A fit of the Hβ line revealed a narrow and broad component, where ${\rm FWHM_{broad}} = 3439 \pm 413\,{\rm km\,s^{-1}}$. This broad component is not present in the well-detected [O III]$\lambda\lambda$4959,5007 lines, implying that it originates from a high-density broad-line region (BLR) of an AGN (e.g. A. Baskin & A. Laor 2005). UNCOVER_20466 is also classified as an AGN based on the narrow emission-line ratio diagnostics proposed by G. Mazzolari et al. (2024).

After correcting for lensing magnification, V. Kokorev et al. (2023) used the relations of J. E. Greene & L. C. Ho (2005) to derive $\log_{10}(M_{\rm BH}/{\rm M}_\odot) = 8.17 \pm 0.42$ (from broad Hβ luminosity and width) and $\log_{10}(M_{\rm BH}/{\rm M}_\odot) = 8.01 \pm 0.40$ (from a calibration based on L_{5100}). Assuming the conservative case of a stellar-only continuum (i.e. no AGN), V. Kokorev et al. (2023) determine $\log_{10}(M_*/{\rm M}_\odot) < 8.7$ (corrected for gravitational lensing). The bolometric luminosity is estimated as $L_{\rm bol} = (6.6 \pm 3.1) \times 10^{45}\,{\rm erg\,s^{-1}}$, using the H$\beta$-based relation of J. Stern & A. Laor (2012).

Together, this suggests that UNCOVER_20466 features an extremely overmassive black hole, undergoing rapid accretion ($\lambda_{\rm Edd} \sim 40$ per cent). This was further explored by H. Zhang et al. (2025), who used the empirical model TRINITY (H. Zhang et al. 2023) to show that the black hole of UNCOVER_20466 is overmassive for its redshift, similar to other high-redshift galaxies detected with *JWST* (e.g. UHZ1; P. Natarajan et al. 2024). While many other overmassive black holes have been discovered at $z > 5$ (e.g. A. D. Goulding et al. 2023; H. Übler et al. 2023; L. J. Furtak et al. 2024; R. Maiolino et al. 2024; H. B. Akins et al. 2025a; F. D'Eugenio et al. 2025a; I. Juodžbalis et al. 2025a; R. Maiolino et al. 2025a; R. P. Naidu et al. 2025a; L. Napolitano et al. 2025; P. Rinaldi et al. 2025b), UNCOVER_20466 remains among the earliest ($z = 8.5$, or ~ 600 Myr after the Big Bang) and

[1] UNCOVER_20466 was given the ID 13 556 in I. Labbe et al. (2025).

Table 1. BlackTHUNDER NIRSpec-IFU observation properties.

Disperser/filter	Readout Pattern	Groups/Int	On-source Time (ks)
G395H/F290LP	NRSIRS2	26	26.8
PRISM/CLEAR	NRSIRS2RAPID	34	7.2

most overmassive ($M_{\rm BH}/M_* \gtrsim 0.06$) black holes in the observable Universe.

In this work, we present new *JWST*/NIRSpec IFU observations of UNCOVER_20466, taken as part of the BlackTHUNDER survey. In Section 2, we detail the *JWST*/NIRSpec IFU data used for this work, as well as archival *JWST*/NIRCam data. Section 3 is an overview of our spectral extraction and fitting routine. We use the best-fitting values to estimate several properties of UNCOVER_20466 in Section 4, and discuss the nature and evolution of this source in Section 5. We conclude in Section 6.

We assume a concordance cosmology throughout, with $H_o = 70\,{\rm km\,s^{-1}\,Mpc^{-1}}$, $\Omega_{\rm m} = 0.3$, and $\Omega_\Lambda = 0.7$. At the redshift of UNCOVER_20466 ($z = 8.50$), 1 arcsec corresponds to 4.63 proper kpc (pkpc). Combining this with the gravitational magnification of UNCOVER_20466 ($\mu = 1.33$; L. J. Furtak et al. 2023a), 1 arcsec in the image plane therefore corresponds to approximately 4.02 pkpc in the source plane. Emission lines are named based on their air wavelength, while we use their vacuum wavelengths for analysis (e.g. $\lambda_{\rm rest,[O\,III]\lambda5007} = 5008.24$ Å).

2 OBSERVATIONS AND DATA REDUCTION

2.1 *JWST*/NIRSpec IFU

The *JWST*/NIRSpec IFU data studied in this work originate from the BlackTHUNDER Large Programme (Black holes in THe early Universe aNd their DensE surRoundings; PID 5015; PIs: H. Übler, R. Maiolino). UNCOVER_20466 was observed on 2024 December 4–5 in PRISM/CLEAR (hereafter R100, $R \sim 30-300$, $0.60\,\mu{\rm m} < \lambda_{\rm obs} < 5.30\,\mu{\rm m}$) and G395H/F290LP (hereafter R2700, $R \sim 2000-3700$, $2.87\,\mu{\rm m} < \lambda_{\rm obs} < 5.14\,\mu{\rm m}$) using a 14-point medium cycling dither pattern (see Table 1 for more observation details).

The raw data from these observations were downloaded from the the Barbara A. Mikulski Archive for Space Telescopes (MAST[2]). Calibration was performed using a customized version of the official pipeline (v1.15.0; H. Bushouse et al. 2025; see M. Perna et al. 2023 for more details of customization) with CRDS context 1293. These customizations account for 1/f noise correction, the subtraction of median values from count rate maps, manually masked cosmic rays and snowballs, open MSA slits, and rejection of artifacts identified by high flux-normalized derivatives along the dispersion direction of the count rate maps (F. D'Eugenio et al. 2024, using a rejection threshold of higher than 99.5 per cent of the resulting distribution for R100, and 98 per cent for R2700). By also utilizing our multiple dithers and the drizzle algorithm (A. S. Fruchter & R. N. Hook 2002), we create two calibrated data cubes with spaxels of 0.05 arcsec. We also removed pixels associated with artifacts by calculating the standard deviation of each spectral channel of the ERR extension (sigma_clipped_stats from astropy.stats).

[2]https://mast.stsci.edu/portal/Mashup/Clients/Mast/Portal.html

Next, we performed background subtraction on each cube using the Background2D task of photutils (L. Bradley et al. 2021). First, the spatial region of UNCOVER_20466 was masked in each cube, in order to exclude the signal from the background estimation. We then use Background2D to divide the field of view into boxes of width 10 px (0.5 arcsec), calculate the sigma-clipped noise level in each box (3σ), spatially smooth the resulting background cube using a square filter of 5 px (0.25 arcsec), and apply a median filter of width 25 spectral pixels to find a final background cube. We inspected both background cubes to ensure that no narrow features were present, and used them to create background-subtracted cubes.

2.2 *JWST*/NIRCam

UNCOVER_20466 was observed with NIRCam as part of two programmes: UNCOVER and 'Medium Bands, Mega Science' (PID 4111; PI: K. Suess; K. A. Suess et al. 2024). Combined, these surveys imaged UNCOVER_20466 in 20 different filters (see Appendix B for details of each filter used in this work). We downloaded all available *JWST*/NIRCam images with stage 3 calibration from the MAST archive.

3 SPECTRAL ANALYSIS

Due to the very compact nature of UNCOVER_20466 with respect to the *JWST*/NIRSpec IFU PSF, we do not spatially resolve the emission. Therefore, our primary analysis is focused on integrated spectra from the R100 and R2700 data cubes. While the field also contains a serendipitous source at lower redshift ('BlackBolt-1', see Appendix C), we defer detailed analysis of this other object to a future work.

3.1 Spectral extraction

The extraction aperture for UNCOVER_20466 should be carefully considered, as it must be small enough to maximize the S/N of each line, but large enough to contain all significant emission. Because UNCOVER_20466 is very compact, it may be considered a point source for our observations, so the observed morphology will be dictated by the PSF. After a thorough exploration of the PSF of our data (see Appendix D1), we proceed with an aperture that captures 60 per cent of the flux of the PSF at the observed wavelength of [O III]λ5007, or a circular aperture of radius 0.125 arcsec centred on the observed emission.

To visualize this aperture, we first create a flux map of [O III]λ5007 by summing the spectral channels of this line ($4.738 < \lambda_{\rm obs}/\mu{\rm m} < 4.793$) in our R100 data cube, creating a similar continuum map by summing adjacent, line-free spectral channels, and subtracting the two to create a line-only map (Fig. 1; e.g. J. Scholtz et al. 2024). We compare the spatial distribution to both our aperture (red circle) and the range of PSF FWHM values in our data as found with STPSF (white circles, see Appendix D1). Note that since the PSF at the wavelengths of other lines (e.g. Ly α, H β) are more compact, we will capture a higher percentage of these fluxes (see Appendix D for details of this aperture loss correction).

We extract spectra from both the R100 and R2700 data cubes using this aperture. Each spectrum is corrected for gravitational magnification (i.e. $\mu = 1.33$, as assumed by V. Kokorev et al. 2023) and aperture loss. As noted by other works (e.g. H. Übler et al. 2023, 2024), the ERR extension of each data cube contains

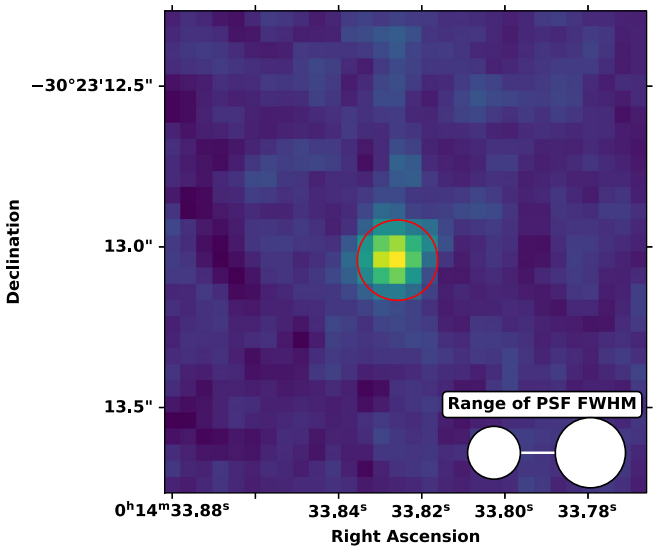

Figure 1. Flux map of [O III]λ5007 in UNCOVER_20466, compared to adopted aperture (red circle) and PSF FWHM range of our data (white circles).

the wavelength-dependent noise variation, but underestimates the true uncertainty. To correct for this, we follow the standard approach of determining the RMS scatter in a spectral range with no significant emission lines and scaling the error spectrum from ERR to feature the same scatter.

3.2 Spectral fitting

Due to the availability of both R100 and R2700 data, we perform spectral fitting in two stages. First, we consider the data bluewards of the Balmer limit ($\lambda_{\rm rest} < 0.3645\,\mu$m; Section 3.2.1), or the location where many LRDs have been observed to feature a change in the spectral slope continuum, resulting in a 'v'-shape (e.g. R. E. Hviding et al. 2025; R. P. Naidu et al. 2025a; D. J. Setton et al. 2025b). This wavelength range is only covered by the R100 data. Next, we consider the data redwards of the Balmer limit, and fit the R100 and R2700 data simultaneously (Section 3.2.2).

3.2.1 Blue fit

First, we consider R100 data between $1050\,\text{Å} \lesssim \lambda_{\rm rest} \lesssim 3645\,\text{Å}$ ($1.00\,\mu\text{m} < \lambda_{\rm obs} < 3.46\,\mu\text{m}$). We note that while this data cube contains data at $\lambda_{\rm obs} < 1.00\,\mu$m, it is excluded due to high noise levels (as seen in the ERR extension of the data).

While the majority of the continuum emission may be described by a power-law model with spectral slope $\beta_{\rm UV}$, the spectral slope here may deviate from the previously measured $\beta_{\rm UV}$ due to contributions from two-photon continuum or damped Lyα clouds (e.g. A. J. Cameron et al. 2024; S. Tacchella et al. 2025). In addition, this spectral region contains the Lyα break which, when observed with the low spectral resolution of the PRISM disperser, may result in an artificial Lyα damping wing (e.g. K. E. Heintz et al. 2024). Thus, we follow the approach of other works (e.g. G. C. Jones et al. 2025a) to model the continuum here, as discussed below.

An initial high-resolution model spectrum is created (channels of width 0.005 μm), and all spectral channels below the observed Lyα wavelength ($\lambda_{\rm obs} < (1+z_{{\rm Ly}\alpha}) \times 0.1216\,\mu$m) are set to a constant value.[3] The continuum between the Lyα break and $\lambda_{\rm rest} = 1500\,\text{Å}$ is modelled as a power law ($F_\lambda \propto \lambda_{\rm obs}^{\beta_{{\rm Ly}\alpha}}$), and Ly$\alpha$ flux is added to the first channel redwards of the Lyα break. The continuum between $\lambda_{\rm rest} = 1500\,\text{Å}$ and the Balmer break is modelled as a separate power law ($F_\lambda \propto \lambda_{\rm obs}^{\beta_{\rm UV}}$), where we enforce continuity at $\lambda_{\rm rest} = 1500\,\text{Å}$.

The resulting continuum and Lyα model is convolved with the wavelength-dependent line spread function (LSF[4]) and rebinned to match the wavelength bins of the observed data. We then add model Gaussians representing C III]λλ1907, 1910 and Mg IIλλ2796, 2803, where the intrinsic widths and redshifts of each line are set to be equal. Due to the spectral resolution of the R100 data, we model each line pair as a single Gaussian. We account for the effect of the LSF by adding the intrinsic linewidth and LSF in quadrature. The free parameters of this approach are the continuum parameters (constant value bluewards of Lyα break, value at $\lambda_{\rm rest} = 1500$Å, $\beta_{{\rm Ly}\alpha}$, $\beta_{\rm UV}$), line fluxes (Lyα, C III]λλ1907, 1910 and Mg IIλλ2796, 2803), and intrinsic linewidths (FWHM$_{\rm N}$).

Previous studies of high-redshift galaxies with *JWST*/NIRSpec have detected strong emission from several rest-UV lines, including C IV λλ1548, 1551, NIV]λ1486, and N III]λ1747-/-1754 (e.g. A. J. Bunker et al. 2023; J. Scholtz et al. 2025a; R. P. Naidu et al. 2025b). While we do not detect these lines in our data, it is possible that they are spread over multiple spectral channels by the wide R100 LSF. To avoid this effect biasing our measurement of the UV spectral slope, we exclude spectral channels within $10^4\,\text{km s}^{-1}$ (corresponding to approximately the FWHM of the LSF at these wavelengths) of each of these lines while fitting the data (see shaded regions in Fig. 2).

We use LMFIT (M. Newville et al. 2014) in 'least_squares' mode to fit the extracted R100 spectrum, using the inverse variance as a weight. Due to the low-spectral resolution of the R100 data, we fixed the redshift of each line and the Lyα break to be $z = 8.50$. Additionally, we fix the intrinsic linewidths to be $250\,\text{km s}^{-1}$. Our fits suggest that Mg IIλλ2796, 2803 is undetected, so we set the flux of this line doublet to 0 in the model and use the error spectrum to derive an upper limit on its flux. The best-fitting parametres are listed in Table 2.

3.2.2 Red fit

Next, we consider data between $3645\,\text{Å} \lesssim \lambda_{\rm rest} \lesssim 5475\,\text{Å}$ ($3.46\,\mu\text{m} < \lambda_{\rm obs} < 5.2\,\mu\text{m}$).[5] This range is covered by both the R100 and R2700 data, so we fit a model to both spectra simultaneously.

The continuum is modelled as a single power-law component ($F_\lambda \propto \lambda_{\rm obs}^{\alpha_{\rm opt}}$), and we include emission from [O II]λλ3727, 3729, [Ne III]λλ3869, 3968, Hδ, Hγ, [O III]λ4363, Hβ, and [O III]λλ4959, 5007. The ratios of [Ne III]λ3869/[Ne III]λ3968 = 3.320 and [O III]λ5007/[O III]λ4959 = 2.983 (which are independent of ISM conditions) are derived using PYNEB (V. Luridiana, C. Morisset & R. A. Shaw 2015). For each Balmer

[3] Ideally, this continuum value below the Lyα break should be zero. However, we allow it to vary to account for calibration or imaging artifacts.
[4] We determine the LSF using the fiducial resolving power curves recorded at https://jwst-docs.stsci.edu/jwst-near-infrared-spectrograph/nirspec-instrumentation/nirspec-dispersers-and-filters.
[5] Similarly to above, we exclude $\lambda_{\rm obs} > 5.20\,\mu$m data due to artifacts created during background subtraction.

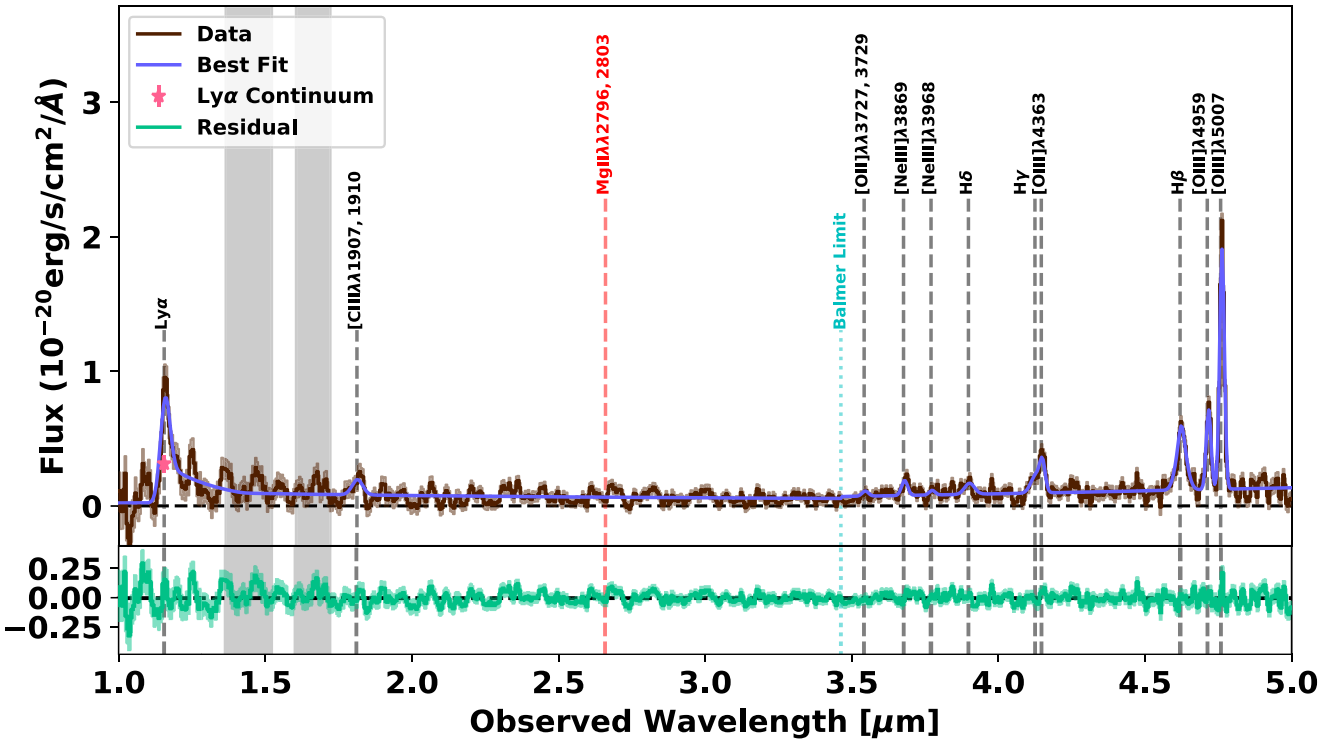

Figure 2. Spectrum extracted from NIRSpec IFU R100 data cube (brown line) using a circular aperture of radius 0.125 arcsec. A concatenation of the best-fitting red model (using R100 data only) and blue model (using R100 and R2700 data) is shown by the blue line, where the dividing wavelength (i.e. the Balmer break) is shown by a dotted cyan line. Model residuals are shown in the lower portion of the panel (green line). The best-fitting centroid wavelengths of the narrow components of each line are shown by dashed vertical black lines, whereas red dashed lines indicate undetected emission lines. The best-fitting continuum underlying Lyα is shown by a pink star. Uncertainties (1σ) for the extracted spectrum and residuals are shown by shaded regions. The wavelength ranges that were excluded from the fit to reduce contamination by faint rest-UV lines are shown by grey-shaded regions.

line (Hδ, Hγ, and Hβ), we include both narrow and broad components. All lines are modelled as Gaussians with the same redshift, while the intrinsic linewidth (FWHM$_{\rm N}$) of all narrow lines are set to be identical. The intrinsic FWHM of the broad component of the Balmer lines are separately set to be identical (FWHM$_{\rm B,Ba}$).

It is important to note that due to flux and wavelength calibration differences, the spectra extracted from JWST/NIRSpec prism and grating data cubes spectra may not yet be compared on a 1:1 basis. Works investigating *JWST*/NIRSpec MSA spectra have found that the medium-resolution ($R\sim1000$) grating flux is $\sim10-15$ per cent higher than the prism flux (but with considerable scatter; e.g. A. J. Bunker et al. 2024; F. D'Eugenio et al. 2025b). The same works also find a redshift difference of $z_{\rm R100}-z_{\rm R1000}\simeq0.004$, which corresponds to a velocity offset of $\sim125\,{\rm km\,s^{-1}}$ at $z=8.5$. Works using both prism and high-resolution ($R\sim2700$) data have found an even higher redshift difference ($z_{\rm R100}-z_{\rm R2700}\simeq0.006-0.009$; P. G. Pérez-González et al. 2025; G. C. Jones et al. 2025b; $\sim190-285\,{\rm km\,s^{-1}}$ at $z=8.5$). The ratio of line fluxes measured in R100 data to those measured in R2700 data has been found to vary widely between NIRSpec IFU observations ($F_{\rm R100}/F_{\rm R2700}\sim0.35-1.70$; S. Arribas et al. 2024; X. Ji et al. 2024, 2025b; J. Scholtz et al. 2025b). With these results in mind, we allow the systemic redshift to vary between the R100 and R2700 data, and include a wavelength-independent flux ratio between the two observed spectra.

Similarly to Section 3.2.1, we use LMFIT in 'least_squares' mode to fit our model to the data. But in this case, we fit the model to both the R100 and R2700 data at the same time. The free parameters are: the continuum slope ($\alpha_{\rm opt}$) and normalization at $\lambda_{\rm rest}=4959$Å ($C_{\rm opt}$), the systemic redshift in each dataset ($z_{\rm R100}$, $z_{\rm R2700}$), the flux ratio of the R100 and R2700 data ($F_{\rm R100}/F_{\rm R2700}$), the intrinsic linewidths of the narrow and broad components (FWHM$_{\rm N}$, FWHM$_{\rm B,Ba}$), and the fluxes of each line ([O II]$\lambda\lambda$3727, 3729, [Ne III]$\lambda\lambda$3869, 3968, [O III]λ4363, [O III] $\lambda\lambda$4959,5007, and the narrow and broad components of Hδ, Hγ, and Hβ). These properties are used to create model R100 and R2700 spectra that account for the LSF, spectral gridding, flux offset, and velocity offset of each dataset. To perform the simultaneous fit, we calculate and concatenate the residual spectrum (i.e. difference between data and model, weighted by the inverse error of each dataset) for each observed spectrum and use LMFIT to find the parameters that minimize this residual.

The flux ratio of [O II]λ3727/[O II]λ3729 is a strong tracer of electron density (e.g. Y. Isobe et al. 2023), varying from 0.67–2.88 for $\log_{10}(n_{\rm e}/{\rm cm^{-3}})=0-8$ (as derived with PYNEB, assuming $T_{\rm e}=10^4$ K). While higher temperatures result in a higher ratio, most of the variation is due to density (e.g. [O II]λ3727/[O II]λ3729 = 0.69–2.96 for the same density range, but assuming $T_{\rm e}=10^7$ K). The R100 data do not resolve the doublet, and the R2700 data do not include a strong detection of both lines. Because of this, it is not possible to place a strong constraint on the [O II]λ3727/[O II]λ3729 ratio as a free parameter. Instead, we tested fits using a range of physically motivated [O II]λ3727/[O II]λ3729 ratios $(0.7, 0.8, \ldots, 3.0)$ and recorded the goodness of fit values for each run (i.e. χ^2, re-

Table 2. Best-fitting emission-line properties, as derived from fits to R100 and R2700 data. The two datasets feature a significant velocity offset ($\Delta v_{\rm R100-R2700}$) and flux ratio ($F_{\rm R100}/F_{\rm R2700}$), which are listed here. Redshift and fluxes are reported as measured in the R100 frame. We mark which properties were derived with the R100 data (second column) and the R2700 data (third column). All values have been corrected for gravitational magnification and aperture losses. For undetected lines, we present 3σ upper limits on their flux. For Lyα, we present both the best-fitting flux ($F_{\rm Ly\alpha}$) and rest-frame equivalent width ($EW_{0,\rm Ly\alpha}$).

Quantity	R100	R2700	Units	This work	V. Kokorev et al. (2023)
$z_{\rm sys}$	X	X	-	8.5095 ± 0.0003	8.502 ± 0.003
$\Delta v_{\rm R100-R2700}$	X	X	[km s^{-1}]	182 ± 10	–
FWHM$_{\rm N}$	X	X	[km s^{-1}]	270 ± 5	203 ± 154
FWHM$_{\rm B,Ba}$	X	X	[km s^{-1}]	2503 ± 176	3439 ± 413
$\beta_{\rm Ly\alpha}$	X		-	-5.7 ± 0.9	–
$\beta_{\rm UV}$	X		-	-0.6 ± 0.1	–
C_{1500}	X		[10^{-20} erg s^{-1} cm^{-2}Å^{-1}]	0.10 ± 0.01	–
$\alpha_{\rm opt}$	X	X	-	1.8 ± 0.2	–
C_{4959}	X	X	[10^{-20} erg s^{-1} cm^{-2}Å^{-1}]	0.12 ± 0.01	–
$F_{\rm Ly\alpha}$	X		[10^{-20} erg s^{-1} cm^{-2}]	256.0 ± 23.2	414.1 ± 85.2
REW$_{\rm Ly\,\alpha}$	X		[Å]	85 ± 19	240 ± 30
$F_{\rm [C\,III]\lambda\lambda1907,1910}$	X		[10^{-20} erg s^{-1} cm^{-2}]	52.1 ± 12.1	–
$F_{\rm Mg\,II\lambda\lambda2796,2803}$	X		[10^{-20} erg s^{-1} cm^{-2}]	< 34.8	62.5 ± 15.1
$F_{\rm [O\,II]\lambda\lambda3727,3729}$	X	X	[10^{-20} erg s^{-1} cm^{-2}]	10.4 ± 2.0	15.0 ± 8.0
$F_{\rm [Ne\,III]\lambda3869}$	X	X	[10^{-20} erg s^{-1} cm^{-2}]	29.3 ± 2.5	62.2 ± 15.4
$F_{\rm H\delta,N}$	X	X	[10^{-20} erg s^{-1} cm^{-2}]	< 23.3	12.2 ± 6.5
$F_{\rm H\delta,B}$	X	X	[10^{-20} erg s^{-1} cm^{-2}]	34.9 ± 5.0	–
$F_{\rm H\gamma,N}$	X	X	[10^{-20} erg s^{-1} cm^{-2}]	< 27.2	–
$F_{\rm H\gamma,B}$	X	X	[10^{-20} erg s^{-1} cm^{-2}]	59.2 ± 7.9	–
$F_{\rm [O\,III]\lambda4363}$	X	X	[10^{-20} erg s^{-1} cm^{-2}]	45.9 ± 3.6	83.0 ± 7.2
$F_{\rm H\,\beta,N}$	X	X	[10^{-20} erg s^{-1} cm^{-2}]	25.0 ± 5.0	78.6 ± 5.9
$F_{\rm H\beta,B}$	X	X	[10^{-20} erg s^{-1} cm^{-2}]	164.8 ± 9.4	232.6 ± 17.3
$F_{\rm [O\,III]\lambda5007}$	X	X	[10^{-20} erg s^{-1} cm^{-2}]	359.6 ± 5.1	412.6 ± 11.3
$F_{\rm R100}/F_{\rm R2700}$	X	X	-	0.85 ± 0.01	–

duced χ^2, and Bayesian Information Criterion [BIC]). The best fit was found to be [O II]λ3727/[O II]λ3729 = 0.7, with increasingly poor fits for higher ratios. Thus, we fix [O II]λ3727/[O II]λ3729 = 0.7 in our model. This corresponds to an estimated density of $\log_{10}(n_{\rm e}/{\rm cm}^{-3}) \sim 1.7$ for $T_{\rm e} \sim 10^4$ K, or $\log_{10}(n_{\rm e}/{\rm cm}^{-3}) \sim 2.4$ for more extreme temperatures ($T_{\rm e} \sim 10^7$ K).

We note that while an initial fit was performed with broad and narrow components for each Balmer line (H β, H γ, and H δ), this resulted in a poor fit. Because Hγ falls into the detector gap for the R2700 data, we cannot measure the narrow component of this line. The fit was improved by including broad components for all three lines, and a narrow component for H β. The narrow component of H β is found to have a flux $\sim 1/6^{\rm th}$ that of the broad component, so our current data do not allow us to detect the narrow components of the weaker H δ or H γ.

3.2.3 Fitting results

Following the fitting procedure of Sections 3.2.1 and 3.2.2, we derive best-fitting continuum and line parameters for UNCOVER_20466 from both the R100 and R2700 data. The resulting R100 and R2700 fits are shown in Figs 2 and 3, respectively. The best-fitting blue and red models for the R100 data are concatenated to create a complete model. The best-fitting values are listed in Table 2.

Both spectra are well fit by the same intrinsic model, but we find a significant velocity offset (182 ± 10 km s^{-1}) and flux ratio (0.85 ± 0.01) between the R100 and R2700 data. As noted in Section 3.2.2, these values are expected from calibration differences. The flux ratio is identical to the value assumed by F. D'Eugenio et al. (2026), and falls within the scatter of $F_{\rm R100}/F_{\rm R2700}$ ratios found by J. Scholtz et al. (2025b). Other works find flux ratios of > 1 (e.g. S. Arribas et al. 2024; X. Ji et al. 2024), which may be due to calibration differences (e.g. updates to calibration files) or an intrinsic scatter in this ratio. The velocity offset corresponds to $z_{\rm R100} - z_{\rm R2700} \simeq 0.006$ (i.e. larger than the uncertainty of the R100-based fit of V. Kokorev et al. 2023; $\delta z = 0.003$), while the flux ratio implies that the grating flux is $\sim$ 17 per cent higher than the prism flux. Each value is comparable to previous results (e.g. A. J. Bunker et al. 2024; P. G. Pérez-González et al. 2025; F. D'Eugenio et al. 2025b; G. C. Jones et al. 2025b). For our analysis, we adopt the redshift and fluxes in the R100 frame.

The residuals in each fit are generally low (i.e. $< 2\sigma$). One exception is the fit of [O III]λ5007 in the R2700 data (Fig. 3), which features a central flux excess with neighbouring negative troughs. This residual pattern has been interpreted to indicate the need for a second Gaussian component, possibly representing an outflow (e.g. M. Ginolfi et al. 2020). This hypothesis is weakened by the fact that the addition of an outflow component to the model did not result in a better fit. Alternatively, it may be an example of the wavelength-dependent continuum oscillations (or 'wiggles') seen in NIRSpec IFU data around bright emission lines (e.g. M. Perna et al. 2023). However, these wiggles are artifacts caused by single-spaxel extraction, and extend over wide swathes of each spectrum. Since we use a circular aperture, and the features are isolated to the proximity of [O III]λ5007, these are likely not wig-

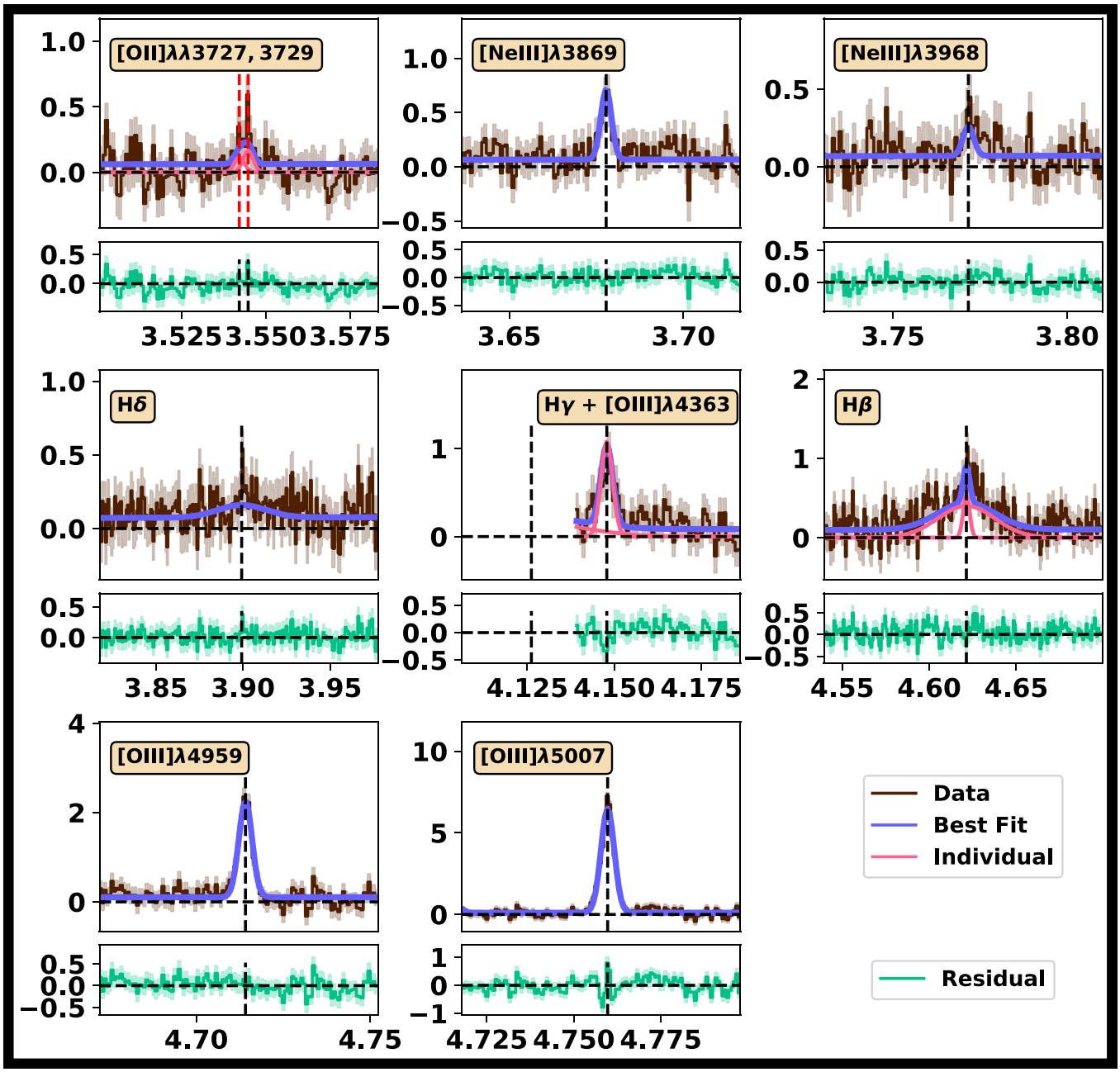

Figure 3. Spectrum extracted from NIRSpec IFU R2700 data cube (brown line) using a circular aperture of radius 0.125 arcsec. The best-fitting model (which was fit to the R100 and R2700 data simultaneously) is shown as blue lines. When two components or lines are overlapping, they are shown by pink lines. Model residuals are shown in the lower portion of each panel (green lines). The best-fitting centroid wavelengths of the narrow components of each line are shown by dashed vertical lines. We only show the wavelength range around emission lines of interest. Uncertainties (1σ) for the extracted spectrum and residuals are shown by shaded regions.

gles. An additional possibility is that these artifacts are caused by a non-Gaussian LSF. In any case, the low amplitude of the residuals allows us to neglect them in our analysis.

In Table 2, we include a comparison to the values of V. Kokorev et al. (2023), who observed UNCOVER_20466 using the *JWST*/NIRSpec MSA in R100. We find that the best-fitting linewidths, redshift, and most emission-line fluxes are in agreement (i.e. within 3σ). Some lines show different flux (as explored in Appendix A), but we find a similar placement of UNCOVER_20466 on the line ratio diagnostic plots of G. Mazzolari et al. (2024), adding credence to the classification of this source as an AGN (Section 4.5).

If we fit the R100 data only, then we measure a $\mathrm{FWHM_{B,Ba}}$ value within 1σ of V. Kokorev et al. (2023) and other works that analysed the R100 data ($\sim 3500\,\mathrm{km\,s^{-1}}$; J. E. Greene et al. 2024; B. Trefoloni et al. 2025). If we fit the R2700 data alone or fit both datasets simultaneously, then a smaller $\mathrm{FWHM_{B,Ba}} \sim 2500\,\mathrm{km\,s^{-1}}$ is preferred (i.e. lower χ^2, reduced χ^2, and Bayesian Inference Criterion). If we instead fix $\mathrm{FWHM_{B,Ba}}$ to the larger value, then the R100 fit is not significantly affected, while the

residuals around the H β line in the R2700 fit are increased. This difference may be affected by the much finer fiducial spectral resolution of the R2700 data at the redshifted wavelength of H β (FWHM$_v \sim 100$ km s^{-1}) versus that of the R100 data (FWHM$_v \sim 1250$ km s^{-1}; where the actual resolution of each dataset could be finer by a factor of $\lesssim 1.7$; e.g. V. Kokorev et al. 2023; A. de Graaff et al. 2024). Alternatively, the LSF could deviate from a perfect Gaussian (which will be investigated in future works). But since the FWHM$_{B,Ba}$ values agree to within 3σ, the R100 data is well fit by either value, and the R2700 data (which features higher spectral resolution) is better fit by the narrower value, we will use this value in our analysis.

4 PROPERTIES OF UNCOVER_20466

The spectral fits of the previous Section result in a number of constraints on line and continuum properties of UNCOVER_20466. Here, we utilize these best-fitting values to characterize the black hole and host galaxy of this system.

4.1 Dust attenuation

Previously, V. Kokorev et al. (2023) measured a best-fitting ratio of Balmer line fluxes ($(F_{H\gamma}/F_{H\beta})_{obs} = 0.31 \pm 0.06$) and derived A_V using:

$$A_V = R_V \frac{2.5}{k(\lambda_{H\beta}) - k(\lambda_{H\gamma})} \log_{10}\left[\frac{(F_{H\gamma}/F_{H\beta})_{obs}}{(F_{H\gamma}/F_{H\beta})_{int}}\right] \quad (1)$$

assuming case B recombination and the reddening law found for the bar of the Small Magellanic Cloud (SMC; K. D. Gordon et al. 2003). This reddening law is commonly adopted for high-redshift quasars (e.g. J. E. Greene et al. 2024; G. Mazzolari et al. 2025; B. Trefoloni et al. 2025; F. D'Eugenio et al. 2025a; X. Ji et al. 2025b). Using this line flux ratio and an intrinsic ratio of $(F_{H\gamma}/F_{H\beta})_{int} = 1/2.14$ results in $A_V = 2.1^{+1.1}_{-1.0}$, or a colour excess of $E(B-V) \equiv A_V/R_V = 0.8 \pm 0.4$. However, the H γ flux used in this calculation included a contribution from the broad component, while the H β flux was from the narrow component only.

We derive further constraints on $E(B-V)$ using all observed Balmer decrements. We only consider pairs of lines from the same emission origin (narrow or broad). The intrinsic ratios are derived using PYNEB, assuming the ISM conditions found for a stack of $4 < z < 7$ Type I AGN from JADES (Y. Isobe et al. 2025, $T_e \sim 2 \times 10^4$ K, $n_e \sim 10^4$ cm^{-3}). As seen in Table 3, we are able to estimate the colour excess of the broad component using three ratios (H δ/H β, H γ/H β, and H δ/H γ). All three of these ratios do not show strong evidence for significant dust attenuation, with $E(B-V)$ values within 2σ of 0. While the small wavelength difference between these lines makes measurement of attenuation more difficult, other JWST/NIRSpec IFU studies of galaxies at $z > 7$ (where Hα is not covered by the nominal wavelength range of JWST/NIRSpec) have found similar results based on Balmer decrements (e.g. A. J. Bunker et al. 2023; G. C. Jones et al. 2024a; S. Zamora et al. 2025a). While we find no significant evidence for reddening in the broad or narrow Balmer lines, we note that JWST/MIRI observations of Hα would enable more precise constraints.

Of course, this result is dependent on a few assumptions. First, we adopt the SMC bar extinction curve of K. D. Gordon et al. (2003). Because each dust attenuation curve is normalized by the value at the approximate wavelength of the Hβ-[OIII]$\lambda\lambda$4959,5007 complex (i.e. V band), the choice of extinction law does not introduce strong changes in the observed values of these lines. As a test, we adopt the starburst reddening law of D. Calzetti et al. (2000), resulting in nearly identical values (i.e. $< 1\sigma$ discrepant). However, we note that the choice of extinction curve will affect the observed rest-UV line fluxes and the continuum slope.

Next, we consider the fact that the intrinsic Balmer ratios are derived using PYNEB and our fiducial ISM conditions. For most densities ($\log_{10}(n_e/\text{cm}^{-3}) \lesssim 6$), these ratios feature a slight dependence on density (e.g. H γ/H β changes by $\lesssim 5$ per cent between $\log_{10}(n_e/\text{cm}^{-3}) = 0$–$7$ and $T_e = (0.5$–$3.0) \times 10^4$ K). At extreme densities ($\log_{10}(n_e/\text{cm}^{-3}) \gtrsim 7$), the ratio transitions to be density dependent. Changing the temperature and density in these ranges does not result in a significant (i.e. $> 1\sigma$) change in the $E(B-V)$ value.

An additional possibility is that we are observing a system where case B recombination is not applicable (e.g. N. Pirzkal et al. 2024; C. Scarlata et al. 2024; W. McClymont et al. 2025; B. Sun & H. Yan 2025). Our observed Balmer decrements suggest minimal dust attenuation (assuming case B), but the fact that our derived $E(B-V)$ values are not significantly negative does not provide strong evidence against case B.

We note that V. Kokorev et al. (2023) reported a large dust attenuation ($A_V \sim 1.9$) from fitting an AGN-only model to the continuum of UNCOVER_20466. At face value, this appears to disagree with the lack of strong attenuation found through analysis of Balmer ratios. However, as noted by other works, AGN-only models return higher dust attenuation than star + AGN models (e.g. G. C. K. Leung et al. 2025). In addition, the Balmer and continuum emission may emerge from different regions, or feature a different geometry. Thus, this difference in A_V could be used as evidence for a stellar component that contributes to the continuum emission, and/or a dusty AGN surrounded by less obscured line-emitting gas.

The non-detection of warm dust emission in a sample of 60 LRDs at $5 \leq z \leq 8$ (C. M. Casey et al. 2025) suggests that this class of objects may not feature significant warm dust reservoirs (i.e. $M_{dust} < 10^6$ M$_\odot$). UNCOVER_20466 only features a single ALMA non-detection, from the Deep UNCOVER-ALMA Legacy High-z (DUALZ) survey (S. Fujimoto et al. 2025). They do not detect significant $\lambda_{obs} = 1.2$ mm emission from UNCOVER_20466, implying a 3σ upper limit of $S_{1.2\,mm} < 99$ μJy. From this single limit,

Table 3. Properties of UNCOVER_20466, as derived from spectral fits to R100 and R2700 data. All values have been corrected for gravitational magnification and aperture losses.

Quantity	This work	V. Kokorev et al. (2023)
$E(B-V)_{H\delta/H\beta,B}$	0.3 ± 0.2	-
$E(B-V)_{H\gamma/H\beta,B}$	0.5 ± 0.3	-
$E(B-V)_{H\delta/H\gamma,B}$	-0.1 ± 0.7	-
$\log_{10}(M_{BH,GH05,H\beta}/M_\odot)$	7.45 ± 0.40	8.17 ± 0.42
$\log_{10}(M_{BH,VP06,H\beta}/M_\odot)$	7.57 ± 0.40	-
$\log_{10}(M_{BH,VP06,5100}/M_\odot)$	7.58 ± 0.40	8.01 ± 0.40
$\log_{10}(L_{bol}/\text{ergs}^{-1})$	44.71 ± 0.02	$45.82^{+0.17}_{-0.28}$
$\log_{10}(L_{Edd,GH05,H\beta}/\text{ergs}^{-1})$	45.6 ± 0.4	-
$\log_{10}(L_{Edd,VP06,H\beta}/\text{ergs}^{-1})$	45.7 ± 0.4	-
$\log_{10}(L_{Edd,VP06,5100}/\text{ergs}^{-1})$	45.7 ± 0.4	-
$\lambda_{Edd,GH05,H\beta}$	$0.15^{+0.23}_{-0.09}$	~ 0.40
$\lambda_{Edd,VP06,H\beta}$	$0.11^{+0.17}_{-0.07}$	-
$\lambda_{Edd,VP06,5100}$	$0.11^{+0.17}_{-0.07}$	-

it is not possible to solve the degeneracy inherent in FIR SED modelling (i.e. between dust temperature $T_{\rm dust}$, dust mass $M_{\rm dust}$, dust emissivity index $\beta_{\rm IR}$).

Assuming a modified blackbody model that accounts for the effect of the CMB at high redshift (e.g. S. Carniani et al. 2019) and adopting a standard value of $\beta_{\rm IR} = 1.8$ suitable for most high-redshift galaxies (e.g. J. Witstok et al. 2023), we find that this observed flux density upper limit does not constrain the dust mass (i.e. even models with $M_{\rm dust} = 10^{10}\,{\rm M}_\odot$ are in agreement) in the case of cold gas ($T_{\rm dust} = 30\,{\rm K}$, or the lower limit for LRDs found by Z. Li et al. 2025). By adopting the conservative limit of $M_{\rm dust} \leq M_* < 10^{9.7}\,{\rm M}_\odot$, we find that the upper limit is only met for $T_{\rm dust} \lesssim 40\,{\rm K}$. Thus, while we may rule out a large reservoir of hot ($T_{\rm dust} > 40\,{\rm K}$) dust, additional ALMA observations (i.e. deeper and at different wavelengths) are required to say more.

4.2 Black hole mass estimation

The black hole mass may be estimated using the properties of the broad Hβ line, which originates from the BLR nearby the black hole, and so-called single-epoch virial relations. The most common method is that of J. E. Greene & L. C. Ho (2005):

$$\log_{10}\left(M_{\rm BH,GH05,H\,\beta}/{\rm M}_\odot\right) = (6.56 \pm 0.02) + (0.56 \pm 0.02)\log_{10}\left(\frac{L_{\rm H\,\beta}}{10^{42}\,{\rm erg\,s^{-1}}}\right) + 2\log_{10}\left(\frac{{\rm FWHM_{H\,\beta}}}{10^3\,{\rm km\,s^{-1}}}\right). \quad (2)$$

We also consider the relations of M. Vestergaard & B. M. Peterson (2006), who derived a similar method based on H β:

$$\log_{10}\left(M_{\rm BH,VP06,H\beta}/{\rm M}_\odot\right) = (6.67 \pm 0.03) + 0.63\log_{10}\left(\frac{L_{\rm H\beta}}{10^{42}{\rm erg\,s^{-1}}}\right) + 2\log_{10}\left(\frac{{\rm FWHM_{H\,\beta}}}{10^3{\rm km\,s^{-1}}}\right) \quad (3)$$

and a relation from the same work that replaces the Hβ luminosity with the continuum emission underlying [O III]λ5007 ($\lambda_{\rm rest} = 5100$ Å):

$$\log_{10}\left(M_{\rm BH,VP06,5100}/{\rm M}_\odot\right) = (6.91 \pm 0.02) + 0.50\log_{10}\left(\frac{\lambda L_\lambda(5100{\rm Å})}{10^{44}{\rm erg\,s^{-1}}}\right) + 2\log_{10}\left(\frac{{\rm FWHM_{H\,\beta}}}{10^3\,{\rm km\,s^{-1}}}\right), \quad (4)$$

where each relation has an intrinsic scatter of ~ 0.4 dex.

We implement these relations with the best-fitting properties of the R100 and R2700 data, resulting in values of $\log_{10}(M_{\rm BH}/{\rm M}_\odot) = 7.4{-}7.6$, with uncertainties of ~ 0.4 dex (i.e. with uncertainties dominated by the scatter of each relation; Table 3). This value is lower than the value of $\log_{10}(M_{\rm BH}/{\rm M}_\odot) = 8.0{-}8.2$ (with uncertainties of ~ 0.4 dex) derived by V. Kokorev et al. (2023), but not significantly ($< 2\sigma$ discrepant). This different value is partially due to the fact that we do not detect significant evidence for dust attenuation from the Balmer decrement, while V. Kokorev et al. (2023) corrected H β using $A_{\rm V} \sim 2$. In addition, the other work found a larger FWHM and line flux of the broad component of H β.

It is worthwhile noting that the single-epoch methods have been calibrated on galaxies in the local Universe, and their application to high-redshift sources is not straightforward. Indeed, recent works have suggested that, for LRDs, the broad emission is due to electron scattering rather than bulk motion around a black hole (V. Rusakov et al. 2025), resulting in a much lower (≥ 2 dex) $M_{\rm BH}$ estimate. As a test, we fit our spectra using the electron scattering assumption, resulting in a slightly better fit (i.e. $\Delta{\rm BIC} \sim 3$). While this would move many high-redshift AGN onto the local $M_{\rm BH}{-}M_*$ relation (see Section 5), this interpretation is the subject of debate (e.g. S. E. I. Bosman et al. 2025; M. Brazzini et al. 2025; I. Juodžbalis et al. 2025a). Thus, we adopt the currently common bulk motion assumption for our analyses. More recently, I. Juodžbalis et al. (2025b) directly measured the black hole mass in a lensed LRD at $z = 7$ by resolving its sphere of influence, finding a mass fully consistent with the virial relations. We consider further these results for our discussion of the black hole versus galaxy properties in Section 5.

4.3 Luminosities and Eddington ratio

The bolometric luminosity can be found from the Hβ broad luminosity using the relation from J. Stern & A. Laor (2012):

$$L_{\rm bol} = 130 \times L_{\rm H\,\beta,B} \times (F_{\rm H\,\alpha}/F_{\rm H\,\beta}), \quad (5)$$

where $(F_{\rm H\,\alpha}/F_{\rm H\,\beta}) = 2.74$ is the intrinsic ratio of these lines, assuming case B recombination and the fiducial ISM conditions of Section 4.1.[6]

We find a value of $\log_{10}(L_{\rm bol}) = 44.72 \pm 0.02$, which is considerably lower than the value of $\log_{10}(L_{\rm bol}) = 45.82^{+0.17}_{-0.28}$ found by V. Kokorev et al. (2023). This difference is partially ascribable to our different treatments of dust attenuation (see Section 4.1). If a high attenuation of $A_{\rm V} = 2$ is taken into account, then the intrinsic Hβ flux increases by a factor of $\sim 20\times$, resulting in higher estimates of $L_{\rm bol}$. Similarly, the higher uncertainty in the previous work is due to the uncertain dust correction, while our value contains no dust correction. As a test, we applied this dust correction to our values, resulting in $L_{\rm bol}$ values within 1σ of V. Kokorev et al. (2023).

Similarly, the Eddington luminosity (e.g. A. C. Fabian 2012) is expressed as

$$L_{\rm Edd} = \frac{4\pi G M_{\rm BH} m_{\rm p} c}{\sigma_{\rm T}} = 1.26 \times 10^{38}\left(\frac{M_{\rm BH}}{{\rm M}_\odot}\right)[{\rm erg\,s^{-1}}]. \quad (6)$$

This is commonly used to calculate the Eddington ratios ($\lambda_{\rm Edd} \equiv L_{\rm bol}/L_{\rm Edd}$). Using the J. E. Greene & L. C. Ho (2005) method to derive black hole mass, we find $\lambda_{\rm Edd} = 0.15^{+0.23}_{-0.09}$ (which is in agreement with the ratios derived using other black hole mass estimation methods). Our ratio is lower than the value of ~ 0.40 measured by V. Kokorev et al. (2023), but due to the large uncertainty on $L_{\rm Edd}$, they are $< 2\sigma$ discrepant. We note that both $L_{\rm bol}$ and $L_{\rm Edd}$ are functions of $L_{\rm H\,\beta}$ (using the calibration of J. E. Greene & L. C. Ho 2005), and a higher H β flux (or a lower FWHM of the broad component of H β) will result in a higher $\lambda_{\rm Edd}$. Since we adopt the same equations, this lower ratio is due to a combination of different dust attenuation assumptions and different aperture loss corrections, as well as the different broad Hβ flux and smaller H β broad linewidth.

4.4 ISM conditions

While the broad emission opens a window into the nature of the black hole of UNCOVER_20466, the narrow lines instead allow

[6] Assuming a higher density ($\log_{10}(n_{\rm e}/{\rm cm^{-3}}) = 7$), as suggested by the analysis Section 4.5, results in a fiducial $(F_{\rm H\,\alpha}/F_{\rm H\,\beta}) = 2.71$, or a decrease of ~ 1 per cent.

us to characterize the host galaxy (or nearby gas; e.g. K. Inayoshi et al. 2025; X. Lin et al. 2025).

To begin, we use our observed line ratios and the code PYNEB to explore the electron density (n_e) through the [O II]$\lambda\lambda$3727, 3729 line pair. As noted in Section 3.2.2, we are not able to directly fit for the ratio of [O II]λ3727/[O II]λ3729 using our data. An exploration of line ratios finds that a low ratio (~ 0.7, implying $\log_{10}(n_e/\mathrm{cm}^{-3}) \sim 2$) yields a better fit. While this ratio has a weak dependence on T_e, a low ratio may only be caused by a low-density environment (i.e. at any temperature).

Next, we consider the [O III]λ4363/[O III]λ5007 ratio, which is a strong indicator of T_e. This ratio is lower in our data (0.13 ± 0.01) than that of V. Kokorev et al. (2023, 0.20 ± 0.02). As noted in V. Kokorev et al. (2023), this ratio is much higher than expected for most galaxies. For an electron density of $n_e \sim 10^{1-4}\,\mathrm{cm}^{-3}$, PYNEB predicts a maximum ratio of $\lesssim 0.05$ for $T_e < 2.5 \times 10^4$ K. While this line ratio is strongly dependent on T_e for $n_e < 10^5\,\mathrm{cm}^{-3}$, it transitions to a strong dependence on n_e for $n_e > 10^5\,\mathrm{cm}^{-3}$. While a ratio of 0.1−0.2 could be theoretically explained by a high density ($n_e \sim 10^6\,\mathrm{cm}^{-3}$) and temperature ($\sim 2 \times 10^4$ K), this density is ~ 2 dex higher than the average value found for $4 < z < 7$ Type I AGN (Y. Isobe et al. 2025) and ~ 3 dex higher than the average value for star-forming galaxies (SFGs) at the redshift of UNCOVER_20466 (e.g. Y. Isobe et al. 2023; S. Li et al. 2025). While high n_e is expected from some interpretations of LRD properties (e.g. V. Rusakov et al. 2025; M. C. Begelman & J. Dexter 2026), these conditions are extreme.

Together, these tracers appear to present contrasting ISM conditions: the low [O II]λ3727/[O II]λ3729 ratio requires low n_e, while the high [O III]λ4363/[O III]λ5007 ratio requires high n_e. One possible explanation is a two-phase ISM, with both low- and high-density emission regions (e.g. X. Ji et al. 2024; Y. Harikane et al. 2025; M. Usui et al. 2025). Alternatively, the [O III]λ4363/[O III]λ5007 ratio could suggest an extraordinarily high temperature (i.e. $> 2 \times 10^4$ K). Similarly high [O III]λ4363/[O III]λ5007 ratios have been observed in other $z > 7$ galaxies (e.g. D. Schaerer et al. 2022; H. Katz et al. 2023; F. Cullen et al. 2025), where they have been explained by a high degree of cosmic ray heating, the presence of high-mass X-ray binaries, or Wolf-Rayet stars. The extreme conditions implied by these ratios independently support the presence of an AGN in this galaxy (see G. Mazzolari et al. 2024; H. Übler et al. 2024, Section 4.5). These aspects will be discussed more thoroughly in the next Section, within the context of AGN and SF photoionization models.

Our observed line fluxes can also be used to estimate the gas-phase metallicity of UNCOVER_20466 using strong line ratio diagnostics (e.g. M. Curti et al. 2020; E. Cataldi et al. 2025). First, we use the calibrations of R. L. Sanders et al. (2024) for SFGs, as they were created using JWST observations of galaxies in a redshift range that contains UNCOVER_20466 (i.e. $2.1 < z < 8.7$). Using the narrow-line flux ratios (O3, O2, R23, O32, Ne3O2, see Table 4 for ratio definitions), we find a best-fitting value of $12 + \log_{10}(O/H) = 7.78 \pm 0.06$, or 0.12 ± 0.02 solar. As an alternative, we consider the rest-UV emission-line metallicity diagnostics for AGN galaxies. If we adopt the calibration of O. L. Dors (2021), which was derived using observations of local Seyfert galaxies, we find a higher metallicity ($12 + \log_{10}(\mathrm{O/H}) = 8.53 \pm 0.12$, or 0.69 ± 0.19 solar). The AGN models of P. Zhu, L. J. Kewley & R. S. Sutherland (2024) instead suggest a $12 + \log_{10}(O/H) = 8.37 \pm 0.10$, or 0.48 ± 0.11 solar.

Table 4. Definitions of line ratios used in this work.

Line ratio	Definition
O3	$F_{[\mathrm{O\,II}]\lambda\lambda 3727,3729}/F_{\mathrm{H}\,\beta}$
O2	$F_{[\mathrm{O\,III}]\lambda 5007}/F_{\mathrm{H}\,\beta}$
R23	$(F_{[\mathrm{O\,II}]\lambda\lambda 3727,3729} + F_{[\mathrm{O\,III}]\lambda\lambda 4959,5007})/F_{\mathrm{H}\,\beta}$
O32	$F_{[\mathrm{O\,III}]\lambda 5007}/F_{[\mathrm{O\,II}]\lambda\lambda 3727,3729}$
Ne3O2	$F_{[\mathrm{Ne\,III}]\lambda 3869}/F_{[\mathrm{O\,II}]\lambda\lambda 3727,3729}$
O3Hg	$F_{[\mathrm{O\,III}]\lambda 4363}/F_{\mathrm{H}\,\gamma}$
O33	$F_{[\mathrm{O\,III}]\lambda 5007}/F_{[\mathrm{O\,III}]\lambda 4363}$

There are caveats with these metallicity derivations, including the possibility that [O II]$\lambda\lambda$3727, 3729 and [O III]$\lambda\lambda$4959, 5007 (which are in every calibration) originate from different components of a multiphase ISM, the possibility that the electron temperature in this object is exceptionally high, or the unproven applicability of metallicity calibration created using SFGs, pure AGN, or local Seyferts to LRDs (e.g. G. Mazzolari et al. 2024).

Most works investigating LRDs assume a low metallicity ($\lesssim$ 20 per cent solar; e.g. C. T. Donnan et al. 2025; D. D. Kocevski et al. 2025), in agreement with the finding of $\lesssim 10$ per cent solar metallicity from individual studies of LRDs (e.g. F. D'Eugenio et al. 2025a; A. de Graaff et al. 2025b; R. Maiolino et al. 2025a). Our SFG-based metallicity estimate is therefore in line with previous findings for high-z LRDs, while the AGN-based calibrations return much higher metallicities. This difference may be caused by a combination of emission from a central AGN and host galaxy (e.g. A. de Graaff et al. 2025a), although this is still under investigation.

If [O III]λ5007 and [O II]$\lambda\lambda$3727, 3729 originate from the same region, we may use our best-fitting line fluxes to estimate a line ratio of O32 $= 34 \pm 9$. This O32 value is larger than the average value found for a sample of $z > 7$ galaxies by M. Tang et al. (2023, ~ 12), and is comparable to the most extreme O32 observed in the $z \sim 4-8$ sample of S. Mascia et al. (2023, ~ 35) and the $z \sim 5.5-9.5$ sample of A. J. Cameron et al. (2023, ~ 30). Our O32 value may then be converted to an approximate ionization parameter U using the photoionization models of C. Morisset et al. (2016), resulting in an approximate value of $\log_{10}(U) = -1.3 \pm 0.3$. This is higher than the standard assumption of $\log_{10}(U) = -2.0$ (e.g. N. Choustikov et al. 2025), and approaches the theoretical limit of $\log_{10}(U) < -1.0$ for H II regions (e.g. S. C. C. Yeh & C. D. Matzner 2012). We emphasize that there are ambiguities concerning these values (O32 and U) due to poor detection of [O II]λ3727 and [O II]λ3729, a possible multiphase ISM, and the use of a photoionization model that may not be appropriate for a high-redshift LRD. Despite this, the fact that [O III]λ5007 is well detected while [O II]$\lambda\lambda$3727, 3729 is not suggests a very high O32 in at least one component of the ISM, and thus a high-level of ionization.

4.5 AGN diagnostics and extreme densities

Since our NIRSpec data do not cover the wavelength range of Hα, [N II]$\lambda\lambda$6548, 6584, or [S II]$\lambda\lambda$6716, 6731, we are unable to investigate the position of UNCOVER_20466 on the commonly used [N II]-BPT (J. A. Baldwin, M. M. Phillips & R. Terlevich 1981) or [SII]-VO87 (S. Veilleux & D. E. Osterbrock 1987) line ratio diagrams. However, a powerful set of alternative diagnostics are those of G. Mazzolari et al. (2024). In ad-

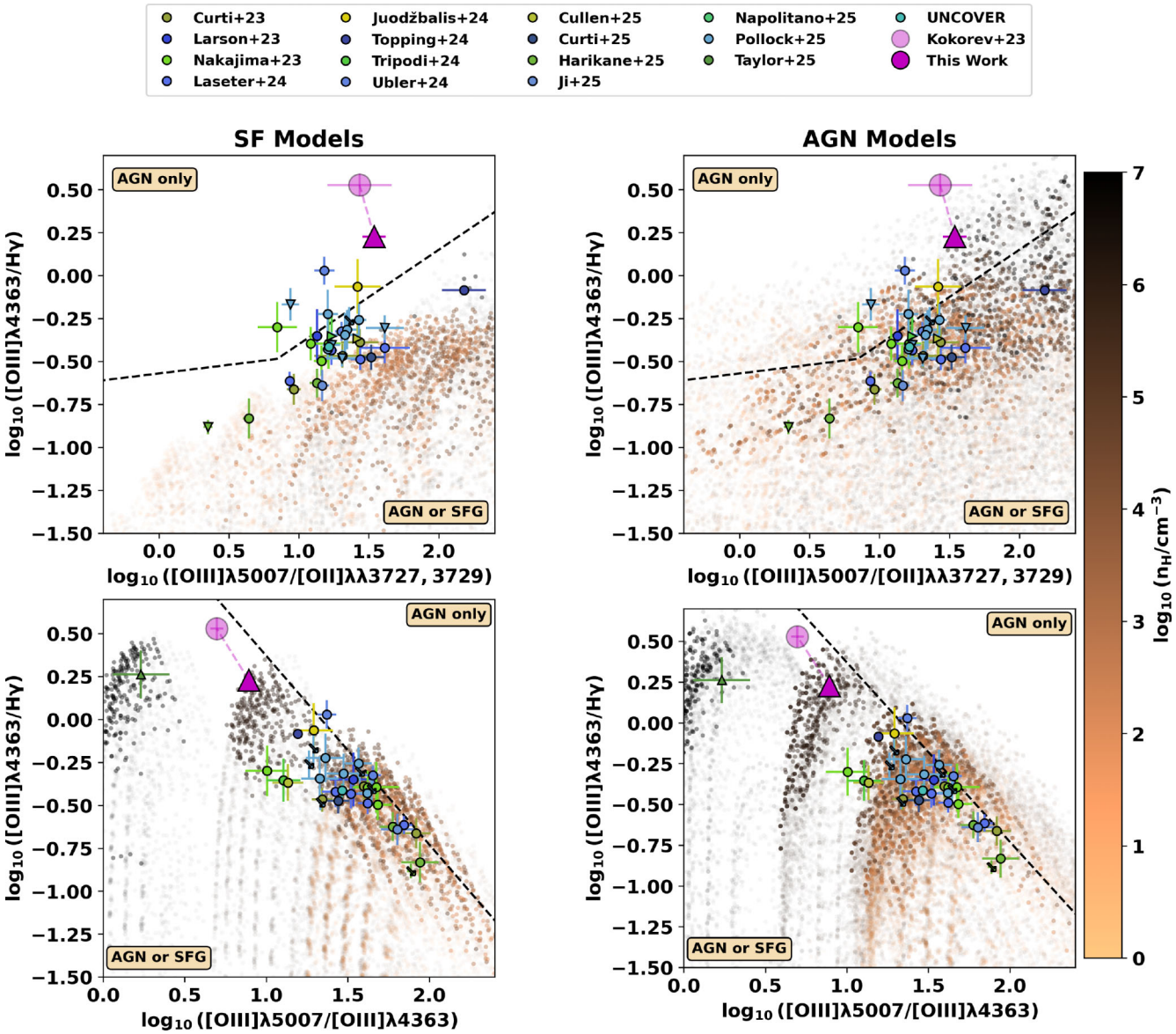

Figure 4. Line ratio diagnostic diagrams of G. Mazzolari et al. (2024), with the value for UNCOVER_20466 from V. Kokorev et al. (2023, magenta circle) and the limit from this work (magenta triangle). Points above each line suggest an AGN-only nature, while those below could be interpreted as AGN or star-forming galaxies (SFGs). For comparison, we include a collection of $z > 6$ measurements (M. Curti et al. 2023; R. L. Larson et al. 2023; K. Nakajima et al. 2023; I. Juodžbalis et al. 2024; I. H. Laseter et al. 2024; R. Tripodi et al. 2024; H. Übler et al. 2024; M. W. Topping et al. 2024a; F. Cullen et al. 2025; M. Curti et al. 2025; Y. Harikane et al. 2025; X. Ji et al. 2025a; L. Napolitano et al. 2025; C. L. Pollock et al. 2025; A. J. Taylor et al. 2025). Values from the HOMERUN models (A. Marconi et al. 2024) are coloured by hydrogen density, with star-forming models in the left column and AGN models in the right column. Models where the density, metallicity, or ionization parameter are comparable to our derived values are shown by darker points, while the fainter points show the full model grid.

dition to O32 and Ne3O2, these diagnostics make use of the [OIII]λ4363 auroral line through O3Hg = [O III]λ4363/H γ and O3 = [O III]λ4363/[O III]λ5007 (Fig. 4). These are used to create line ratio diagrams, with regions in which only AGN are found, while other parts of the diagrams are populated by both AGN and star-forming galaxies.

Previously, G. Mazzolari et al. (2024) used the measured values of V. Kokorev et al. (2023) to show that UNCOVER_20466 was indeed an AGN. Our newly measured line fluxes confirm this (Fig. 4). While the H γ flux reported by V. Kokorev et al. (2023) include contributions from both the narrow and broad components, we only use the 3σ upper limit on the narrow component of H γ (Table 2[7]) to find a similar result. Our limit lies below the demarcation line for the O3Hg − O33 plot (lower panels of Fig. 4), but does not disagree with an AGN interpretation, given that this lower region is populated both by AGN and SF galaxies.

To place this in a broader context, we compare the location of UNCOVER_20466 in these line ratio diagrams to those of high-redshift ($z > 6$) sources from literature (M. Curti et al. 2023; R. L. Larson et al. 2023; K. Nakajima et al. 2023; I. Juodžbalis et al.

[7]Note that since H γ falls in a spectral gap of the R2700 data, this upper limit is dependent on the R100 data.

2024; I. H. Laseter et al. 2024; H. Übler et al. 2024; M. W. Topping et al. 2024a; F. Cullen et al. 2025; M. Curti et al. 2025; Y. Harikane et al. 2025; X. Ji et al. 2025a; C. L. Pollock et al. 2025; A. J. Taylor et al. 2025). We also collect all sources from UNCOVER DR4 (R. Bezanson et al. 2024; S. H. Price et al. 2025)[8] with significant line detections, resulting in one additional source (UNCOVER_10646, $z = 8.5$). From this comparison, it is clear that UNCOVER_20466 features one of the highest O3Hg ratios among the observed galaxies. A rare exception in this sample is the upper limit of CAPERS-LRD-z9 (A. J. Taylor et al. 2025), which is comparable to ours. This source also features a very low O33, implying a high [O III]λ4363/[O III]λ5007 ratio of ~ 0.6. As discussed in Section 4.4, even our estimated [O III]λ4363/[O III]λ5007 ratio of ~ 0.1 is difficult to explain without requiring extreme conditions (i.e. unphysically high temperature or density). While CAPERS-LRD-z9 is a BL LRD with a similar $M_{\rm BH}$ (see Section 5.2), it lies far from the AGN demarcation line in the O3Hg − O33 diagnostic plot. Thus, UNCOVER_20466 remains one of the most clear AGN in these diagnostics.

The faint coloured points in each panel represent line ratios from a large library of single-cloud CLOUDY (G. J. Ferland 1993; G. J. Ferland et al. 2017) models used by A. Marconi et al. (2024) and M. Ceci et al. (2025) for the 'Highly Optimized Multicloud Emission-line Ratios Using photo-ionizatioN' (HOMERUN) model. The star-forming galaxy CLOUDY models (left column) were computed with the following parameters. The ionizing continua are from stellar population models from BPASS v2.3 (E. R. Stanway & J. J. Eldridge 2018; C. M. Byrne et al. 2022) including binary stellar evolution and use a P. Kroupa (2001) initial mass function with an upper mass cut-off of 300 $M_\odot$. The modelled stellar populations featured metallicities $\log_{10}(Z_\star) = -1.7$(solar), −2.7, −4.0, −5.0 and ages in $\log_{10}$(age/Myr) = 6.0, 6.4, 6.6, 7.1, 8.0. The ionized gas has ionization parameter $\log_{10}(U)$ ranging from –4.0 to –0.5 in steps of 0.5, constant gas density $\log_{10}(N_{\rm H}/{\rm cm}^{-3})$ ranging from 0 to 7 in steps of 1, and metallicities $\log_{10}(Z_{\rm gas}/Z_\odot)$ ranging from −4.3 to 0.4 in steps of 0.2 (with the constraint that the gas metallicity is within a factor 0.1 and 100 of the stellar metallicity). Models were considered both with and without dust.

The ionizing continuum for the AGN models (right column) is described by a power law with UV slope $\alpha_{\rm UV} = -0.5$, an exponential cut-off $\exp(-h\nu/kT_{\rm max})$ and an X-ray power-law with slope of $\alpha_{\rm UV} = -1.0$ linked to the UV through the $\alpha_{\rm ox}$ parameter. Models were computed with combinations of $\log_{10}(T_{\rm max}/{\rm K}) = 4.0, 4.5, 5.0, 5.5, 6.0, 6.5, 7.0$ and $\alpha_{\rm ox} = -1.2, -1.5, -1.8$. The other parameters are the same with the exception that the ionization parameter upper limit is 0.5 and that the gas metallicity always cover the range of $-2 \leq Z/Z_\odot \leq 1.0$ with steps of 0.2.

The full grid of CLOUDY models spans a wide range of physical parameters, many of which unlikely to be applicable to UNCOVER_20466. For clarity, we isolate a subset of the models ($2 < \log_{10}(N_{\rm H}) < 7, -1.5 < \log_{10}(U) < -1.0, -1.0 < \log_{10}(Z) < 0.0$) that approximate the properties of our source as found in Section 4.4 ($\log_{10}(n_{\rm H}) \sim 2-7$ from our analyses of the [O II]λλ3727, 3729 doublet and [OIII]λ4363/[O III]λ5007 ratio, $\log_{10}(U) = -1.3 \pm 0.3$ from O32, and $\log_{10}(Z) \sim -0.2$ to −0.9 depending on calibration). This subset is shown in Fig. 4 as darker points.

[8] https://jwst-uncover.github.io/DR4.html

The comparison of these SF (left panels) and AGN models (right) clearly indicate that these diagrams (and especially O3Hg vs O32) are extremely effective in identifying AGN, and that the dividing line between AGN-only and AGN + SF regions is likely very conservative. It is noticeable that even extremely high densities are not enough to reach high [O III]λ4363/H γ values (at a given O32 value) when considering SF galaxies. In order to reach very high [O III]λ4363/H γ the presence of an AGN is needed, likely because the hard AGN radiation field is very effective in heating the ISM, hence boosting the flux of the corona line.

The specific case of UNCOVER_20466 is particularly intriguing, as it requires not only AGN photoionization but also extremely high densities, of about 10^7 cm^{-3}. Together with the fact that this is the one of the most distant sources in the sample shown, this may indicate that UNCOVER_20466 is forming embedded in the very dense gas of an early protogalaxy.

Recently, E. Lambrides et al. (2025) analysed JWST/NIRSpec MSA data of the $z = 6.68476$ LRD THRILS_46403 (also known as CEERS-10444; D. D. Kocevski et al. 2025), revealing evidence for a very high $\log_{10}$(O3Hg) = 1.16 ± 0.06. This ratio is higher than observed in UNCOVER_20466, and is also ~ 0.5 dex higher than the most extreme HOMERUN AGN models, suggesting uncommon conditions. However, we note the strong Balmer absorption observed in this source is not included in the Hγ line fit, resulting in an overestimation of the O3Hg ratio; additionally prominent FeII emission lines are observed in the spectrum, implying that the [OIII]λ4363 is also likely contaminated by FeII. Even taking these aspects into account, THRILS_46403 represents an extreme galaxy similar to UNCOVER_20466.

4.6 Dynamical mass

To constrain the dynamical mass of the UNCOVER_20466 host galaxy, we use the same relation as H. Übler et al. (2023):

$$M_{\rm dyn} = K(n)K(q)\sigma_*^2 r_{\rm e}/G, \quad (7)$$

where n is the Sérsic index, q is the axis ratio, and $K(n) = 8.87 - 0.831n + 0.0241n^2$ and $K(q) = \left[0.87 + 0.38e^{-3.71(1-q)}\right]^2$ are taken from M. Cappellari et al. (2006) and A. van der Wel et al. (2022), respectively. To convert our integrated narrow gas emission linewidth (see FWHM$_{\rm N}$ in Table 2) to an integrated stellar velocity dispersion (σ_*), we adopt the empirical relations for $z \sim 1$ galaxies of R. Bezanson et al. (2018) (as done by other works, e.g. H. Übler et al. 2023). This results in $\sigma_* \simeq 1.26 \times {\rm FWHM_N}/2.355$, or $\sigma_* = 144.3 \pm 2.7$ km s^{-1}.

This mass is dependent on three morphological properties (n, q, $r_{\rm e}$), which we determine from the JWST/NIRCam images using PYSERSIC (I. Pasha & T. B. Miller 2023) and the empirical PSFs. Of the 20 available NIRCam images, we exclude those with a weak detection of UNCOVER_20466, as quantified by a best-fit flux that is less than 3× the associated uncertainty (F182M, F090W, F140M, F150W2-F162M, F210M, F250M, F070W). Using the results of the remaining images, we measure the inverse variance-weighted mean aspect ratio ($q = 0.32 \pm 0.13$), Sérsic index ($n_{\rm s} = 4.9 +/- 0.9$), and magnification-corrected effective radius ($r_{\rm e} = 0.18 \pm 0.06$ kpc). This radius is in agreement with the value derived through a similar analysis by V. Kokorev et al. (2023, $r_{\rm e} = 0.165 \pm 0.020$ kpc) and the mean radius of a sample of more than 200 LRDs by Y. Zhang et al. (2025, 0.21 ± 0.03 kpc in F444W). Adopting our best-fit mean NIRCam morphological parameters, we estimate $\log_{10}(M_{\rm dyn}/M_\odot) = 9.6^{+0.1}_{-0.2}$.

4.7 Lyα properties

As noted in previous works (e.g. V. Kokorev et al. 2023; S. Fujimoto et al. 2024), UNCOVER_20466 is a powerful Lyα emitting galaxy (LAE). The presence of another nearby LAE (within a projected distance of < 500 kpc and redshift difference $\Delta z \sim 0.01$ or $\Delta v \sim 300\,\mathrm{km\,s^{-1}}$) suggests that both LAEs reside in the same ionized bubble (S. Fujimoto et al. 2024). We recover a lower Lyα flux ($2.60 \pm 0.23 \times 10^{-18}$ erg s^{-1} cm^{-2}) and equivalent width (91 ± 20Å) than previous results (e.g. V. Kokorev et al. 2023), but the resulting emission still meets the most conservative criterion for strong Lyα emission used by many studies (i.e. $EW_{0,\mathrm{Ly}\alpha} > 75$Å; e.g. D. P. Stark et al. 2010; L. Pentericci et al. 2018; G. C. Jones et al. 2025a).

From the R100 spectrum, we are able to estimate the Lyα escape fraction. The intrinsic ratio of Lyα/Hβ = 31.87 is estimated using our fiducial ISM conditions (see Section 4.1) and PYNEB. Based on the best-fitting fluxes of the narrow Hβ and Lyα emission (with no dust correction, see Section 4.1), this results in $f_{\mathrm{esc}}^{\mathrm{Ly}\alpha} = 33 \pm 7$ per cent. We note that this commonly applied definition of $f_{\mathrm{esc}}^{\mathrm{Ly}\alpha}$ (e.g. G. C. Jones et al. 2025a; S. Shimizu et al. 2025;) includes the effect of Lyα scattering at multiple scales (e.g. ISM, IGM). If we instead assume a high density of $\log_{10}(n_e/\mathrm{cm}^{-3}) = 7$, then PYNEB outputs a higher intrinsic ratio of Lyα/Hβ = 35.49, resulting in a $< 1\sigma$ lower value of $f_{\mathrm{esc}}^{\mathrm{Ly}\alpha} = 29 \pm 6$ per cent. We find that UNCOVER_20466 falls on the strong correlations between $EW_{0,\mathrm{Ly}\alpha}$-$f_{\mathrm{esc}}^{\mathrm{Ly}\alpha}$ (e.g. R. Begley et al. 2024; I. Goovaerts et al. 2024) and $EW_{0,\mathrm{Ly}\alpha}$–M_{UV} measured by other works (e.g. G. C. Jones et al. 2025a), as shown in Appendix E.

We also note that previous works found a link between O32 (tracing ionization parameter) and $f_{\mathrm{esc}}^{\mathrm{Ly}\alpha}$ (e.g. K. Nakajima & M. Ouchi 2014; H. Yang et al. 2017; N. Roy et al. 2023, but see also e.g. Y. I. Izotov et al. 2020; A. Saxena et al. 2024b). Our high values (see Section 4.4 for O32 details) would appear to support this correlation, lying just beyond the scatter of values from other high-redshift works (e.g. N. Roy et al. 2023).

Some of the properties of UNCOVER_20466 (e.g. compact morphology, high Lyα escape fraction, nearby LAEs, high ionization parameter traced by O32) are also seen in the $z \sim 8.3$ metal-poor LAE CANUCS-A370-z8-LAE (C. J. Willott et al. 2025). But this other source is not an LRD, as it lacks broad Balmer emission or a v-shaped continuum. In addition, it is more metal poor. This highlights the diversity of strong LAEs in the early Universe.

4.8 Continuum properties

Based on JWST/NIRCam photometry, this source was classified as an LRD (I. Labbe et al. 2025). One of the defining characteristics of these objects is a v-shaped continuum, with a negative (positive) F_λ slope in the rest-UV (rest-optical). This was confirmed by the JWST/NIRSpec observations of J. E. Greene et al. (2024), who found $\alpha_{\mathrm{opt}} = 0.5 \pm 0.3$ and $\beta_{\mathrm{UV}} = -0.7 \pm 0.2$ (i.e. the 'red' nature is not due solely to emission lines). Our fits of the R100 spectrum return a redder optical slope ($\alpha_{\mathrm{opt}} = 1.8 \pm 0.2$) and a similar UV slope ($\beta_{\mathrm{UV}} = -0.6 \pm 0.1$). We note that these slopes meet the LRD criteria of $\alpha_{\mathrm{opt}} > 0$ and $-2.8 < \beta_{\mathrm{UV}} < -0.37$ used by classification studies (e.g. K. N. Hainline et al. 2025; D. D. Kocevski et al. 2025), confirming the LRD nature of UNCOVER_20466.

Because we fit the R100 spectrum in two parts (i.e. before and after the Balmer limit), there is a discontinuity at $\lambda_{\mathrm{rest}} = 0.3645\,\mu$m with a red/blue flux ratio of 1.3 ± 0.2 (using the best-fitting values and uncertainties of each continuum model). Balmer breaks are commonly observed in LRDs (e.g. A. de Graaff et al. 2025b; L. J. Furtak et al. 2025; X. Ji et al. 2025b; H. Liu et al. 2025; B. Wang et al. 2025), and this ratio falls within the lower end of the scatter for observed Balmer breaks at high redshift (e.g. A. Kuruvanthodi et al. 2024; A. Vikaeus et al. 2024; B. Wang et al. 2024; M. Tang et al. 2025). However, the current data are not able to confirm a Balmer break in UNCOVER_20466.

5 DISCUSSION

5.1 Black hole–host galaxy scaling relations

Our derived properties allow us to consider the placement of UNCOVER_20466 on planes of M_{BH} as a function of M_*, σ_*, and M_{dyn} (Fig. 5), which will inform us on the evolutionary state of the object. In each panel, we compare the placement of UNCOVER_20466 relative to other *JWST*-AGN at $z > 5$ (A. D. Goulding et al. 2023; Y. Harikane et al. 2023; D. D. Kocevski et al. 2023; R. L. Larson et al. 2023; H. Übler et al. 2023; J. Chisholm et al. 2024; L. J. Furtak et al. 2024; R. Maiolino et al. 2024; H. B. Akins et al. 2025a; F. D'Eugenio et al. 2025a; T. Kiyota et al. 2025; R. P. Naidu et al. 2025a; L. Napolitano et al. 2025; I. Juodžbalis et al. 2025a; R. Maiolino et al. 2025a; P. Rinaldi et al. 2025b; A. J. Taylor et al. 2025; R. Tripodi et al. 2025; J. Zhang et al. 2025), as well as correlations found for low-redshift galaxies (J. Kormendy & L. C. Ho 2013; A. E. Reines & M. Volonteri 2015; J. E. Greene, J. Strader & L. C. Ho 2020; V. N. Bennert et al. 2021).

First, we consider the distribution of black hole mass as a function of stellar mass (Fig. 5a). Most *JWST*-detected black holes lie above the local relation, reflecting overmassive black holes. Our new M_{BH} value is lower than that of V. Kokorev et al. (2023), but it is clear that the black hole of UNCOVER_20466 is overmassive, similar to many *JWST*-detected AGN ($M_{\mathrm{BH}} \gtrsim 0.1 \times M_*$). This is especially evident when comparing to the A. E. Reines & M. Volonteri (2015) local relation, which is calibrated primarily on AGNs. Even if our single-epoch black hole mass would be overestimated by ~ 0.7 dex, as possibly indicated by the recent results for a highly super-Eddington black hole at $z \sim 2.3$ (R. Abuter et al. 2024), UNCOVER_20466 would remain overmassive in the black hole mass–stellar mass plane. Furthermore, the low Eddington ratio we find in this work suggests that a possible correction towards lower black hole masses may not be as large (see discussion by R. Abuter et al. 2024). Additionally, the finding by I. Juodžbalis et al. (2025b) that the direct BH mass measurement in a LRD at $z = 7$ being consistent with local virial relations, supports the idea that the BH mass inferred by us in UNCOVER_20466 is reasonably accurate.

The relation between black hole mass and galaxy velocity dispersion (also known as the 'M–σ' relation, Fig. 5b) has been found to be constant over a range of redshifts ($z < 1$; e.g. Y. Shen et al. 2015). This connection represents a coeval evolution of the black hole and the material surrounding it. As already pointed out by R. Maiolino et al. (2024) and I. Juodžbalis et al. (2025a), most of the JWST-detected AGN fall onto the local correlation, including UNCOVER_20466. One minor note is that the σ_* measured from JWST data represents the narrow linewidth from the full source (corrected for instrumental broadening and converted to stellar dispersion), while the same value from local galaxies is extracted only from the bulge. However, most galaxies entering the local relation are ellipticals or bulge-dominated galaxies, i.e. where the bulge contains most of the stellar mass.

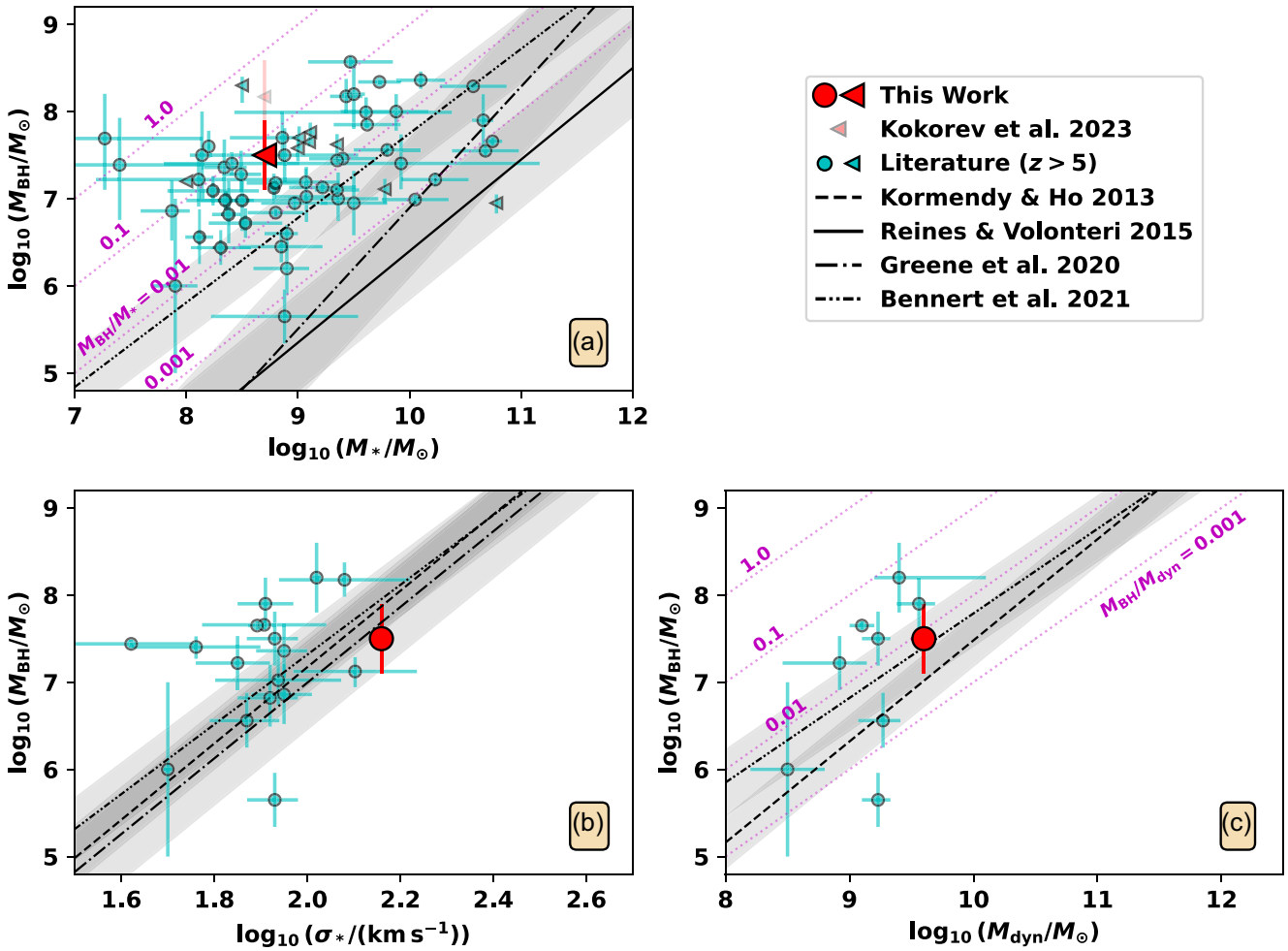

Figure 5. Placement of UNCOVER_20466 on planes of $M_{\rm BH}$–M_* (panel a), $M_{\rm BH}$–σ_* (panel b), and $M_{\rm BH}$–$M_{\rm dyn}$ (panel c, red point). For comparison, we include a sample of $z > 5$ AGN studied with JWST (A. D. Goulding et al. 2023; Y. Harikane et al. 2023; D. D. Kocevski et al. 2023; R. L. Larson et al. 2023; H. Übler et al. 2023; J. Chisholm et al. 2024; L. J. Furtak et al. 2024; R. Maiolino et al. 2024; H. B. Akins et al. 2025a; F. D'Eugenio et al. 2025a; I. Juodžbalis et al. 2025a; T. Kiyota et al. 2025; D. D. Kocevski et al. 2025; R. Maiolino et al. 2025a; R. P. Naidu et al. 2025a; L. Napolitano et al. 2025; P. Rinaldi et al. 2025b; A. J. Taylor et al. 2025; R. Tripodi et al. 2025; J. Zhang et al. 2025). These values are compared to best-fitting relations from local galaxies (J. Kormendy & L. C. Ho 2013; A. E. Reines & M. Volonteri 2015; J. E. Greene et al. 2020). The previous estimate of $M_{\rm BH}$ from V. Kokorev et al. (2023) is included in the $M_{\rm BH}$–M_* plot.

The last correlation is between black hole mass and dynamical mass (Fig. 5c). The JWST-detected AGN are scattered on both sides of the local relation, and UNCOVER_20466 agrees with the V. N. Bennert et al. (2021) relation.

We note that each of the low-redshift correlations originates from different samples. The $M_{\rm BH}$–σ_* and $M_{\rm BH}$–$M_{\rm dyn}$ correlations of J. Kormendy & L. C. Ho (2013) are found using a sample of local elliptical and bulge galaxies, where $M_{\rm dyn} = M_{\rm bulge}$. Similarly, J. E. Greene et al. (2020) fit $M_{\rm BH}$-σ_* and $M_{\rm BH}$-M_* using a sample of local spiral and elliptical galaxies. The sample used to derive the $M_{\rm BH}$–M_* relation of A. E. Reines & M. Volonteri (2015) consisted of local broad line AGN. V. N. Bennert et al. (2021) combined local broad line AGN and quiescent galaxies to examine all three correlations. Since their data allow for the spatial decomposition of the bulge and disc of each source, $M_{\rm dyn}$ is derived using the radius and velocity dispersion of the central bulge. On the other hand, the observed values for high-redshift galaxies are derived in similar ways.

Fig.5(a) shows that UNCOVER_20466 has an overmassive black hole (with respect to the stellar mass), especially compared to AGN in the local Universe. Despite this, it already lies on correlations between $M_{\rm BH}$ and bulge properties (velocity dispersion and dynamical mass, Figs 5b,c). The fact that UNCOVER_20466 falls on the same correlations suggests that it may evolve along those relations into a present-day massive early-type galaxy.

5.2 Black hole growth through cosmic time

It is clear that UNCOVER_20466 features a significant black hole mass at an early cosmic epoch ($t_{\rm H} \sim 580$ Myr). To explore this further, we compare the black hole mass to those of other $z > 6$ AGN (Fig. 6).

First, we consider a simple model for how a black hole will grow through cosmic time. Their growth rate may be derived using their Eddington luminosity and Eddington ratio (e.g. L.-X.

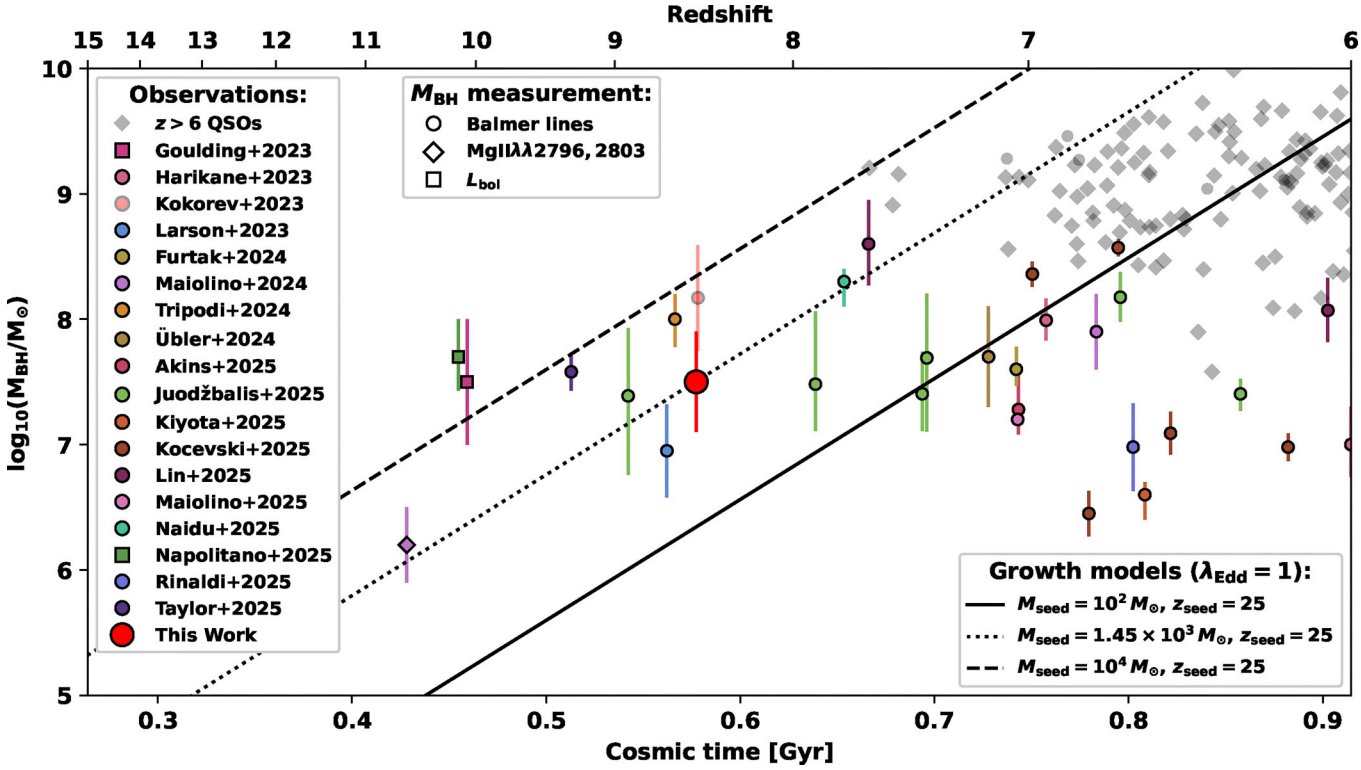

Figure 6. Distribution of black hole masses as a function of cosmic time. Our derived mass for UNCOVER_20466 is shown by a large red circle, while a faint circle shows the previously determined value of V. Kokorev et al. (2023). We include a collection of $z > 6$ QSOs (X. Fan, E. Bañados & R. A. Simcoe 2023; M. A. Marshall et al. 2023; M. Onoue et al. 2025; M. A. Marshall et al. 2025a) and AGN observed by *JWST* (A. D. Goulding et al. 2023; Y. Harikane et al. 2023; R. L. Larson et al. 2023; L. J. Furtak et al. 2024; R. Maiolino et al. 2024; H. Übler et al. 2024; H. B. Akins et al. 2025a; I. Juodžbalis et al. 2025a; T. Kiyota et al. 2025; D. D. Kocevski et al. 2025; R. Maiolino et al. 2025a; R. P. Naidu et al. 2025a; L. Napolitano et al. 2025; P. Rinaldi et al. 2025b; A. J. Taylor et al. 2025; R. Tripodi et al. 2025) for comparison. Galaxies where $M_{\rm BH}$ was found through Balmer line (i.e. H α or H β) scaling relations are shown by circles, while diamonds show where Mg II$\lambda\lambda$2796, 2803 scaling relations were used, and studies that used bolometric luminosity scaling relations are shown as squares. Three simple growth models with different seed masses assuming a seeding redshift of 25 and constant Eddington-limited accretion are plotted as black lines.

Li 2012):

$$\dot{M_{\rm BH}} = \frac{\lambda_{\rm Edd} L_{\rm Edd}}{\epsilon_o c^2} \tag{8}$$

where ϵ_o is the efficiency at which mass is converted to luminosity (here assumed to be 0.1; e.g. S. E. I. Bosman et al. 2025). If each black hole has mass $M_{\rm seed}$ at cosmic time $t_{\rm seed}$ and we assume Eddington-limited accretion ($\lambda_{\rm Edd} = 1$), then we may solve the above equation to determine the mass evolution:

$$M_{\rm BH}(t) = M_{\rm seed} e^{(t - t_{\rm seed})/0.045\,{\rm Gyr}} \tag{9}$$

We use this equation to calculate three growth curves for seeds at $z = 25$: a direct collapse black hole with $M_{\rm seed} = 10^4\,{\rm M}_\odot$, a supermassive star with $M_{\rm seed} = 10^2\,{\rm M}_\odot$, and a seed tuned to match the observed properties of UNCOVER_20466 ($M_{\rm seed} = 1.45 \times 10^3\,{\rm M}_\odot$).

When compared to the literature, UNCOVER_20466 is one of the highest-redshift massive black holes, lying close to other sources at $t_{\rm H} \sim 0.5 - 0.6$ Gyr (i.e. R. L. Larson et al. 2023; R. Tripodi et al. 2024; A. J. Taylor et al. 2025; I. Juodžbalis et al. 2025a). The black hole masses of these sources (which were also derived using Balmer line scaling relations) lie between the growth curves for the $10^2\,{\rm M}_\odot$ and $10^4\,{\rm M}_\odot$ seeds.

The application of $M_{\rm BH}$ scaling relations based on broad Balmer emission is limited by the maximum $\lambda_{\rm obs}$ of the data. Using the standard R100 wavelength limit of $\lambda_{\rm obs} = 5.30\,\mu$m, H α may only be observed up to $z < 7.07$, while H β may be observed up to $z < 9.90$. Recent works have successfully extended the wavelength range of *JWST*/NIRSpec data to $\lambda_{\rm obs} \lesssim 5.5\,\mu$m (e.g. C. T. Donnan et al. 2025; F. D'Eugenio et al. 2025a; see also Dawn *JWST* Archive[9] v4 NIRSpec data release), which allows for Hα and Hβ detection to higher redshifts. Balmer lines at even higher redshifts can be explored using the broad wavelength coverage of *JWST*/MIRI (e.g. C. Prieto-Jiménez et al. 2025). While lower-order Balmer lines (e.g. H γ, H δ) are theoretically observable at higher redshift, their intrinsic faintness relative to H α and H β make their detection difficult.

Instead, the black holes of higher-redshift galaxies may be measured in other ways. Three $z > 10$ AGN have been characterized, where two of them feature similar black hole masses to UNCOVER_20466 (A. D. Goulding et al. 2023; L. Napolitano et al. 2025). Due to the lack of observed Balmer lines, these masses were estimated using $L_{\rm bol}$ relations. In addition, both are X-ray luminous, suggesting a different nature than LRDs. Finally, the currently highest-redshift black hole (GN-z11; R. Maiolino et al. 2024) was estimated using a MgII scaling relation, but falls on the same growth curve as UNCOVER_20466.

[9] https://dawn-cph.github.io/dja/

5.3 Evolution of UNCOVER_20466

Here, we synthesize the previous subsections to consider the past and future evolution of UNCOVER_20466. The correlation plots of Section 5.1 show that UNCOVER_20466 features a black hole that is overmassive compared to its stellar mass, while it lies on the $M_{\rm BH}-\sigma_*$ and $M_{\rm BH}-M_{\rm dyn}$ relations. Combined with the significant broad component of Hβ (FWHM$_{\rm B,Ba}\sim 2500\,{\rm km\,s^{-1}}$) and low Eddington ratio ($\sim$ 10 per cent), this can be interpreted as evidence for rapid black hole accretion in the past (accompanied by low SFR, or small change in M$_*$) which has declined.

Through a comparison of the UNCOVER_20466 black hole mass to model and literature values, we find that while our $M_{\rm BH}$ for UNCOVER_20466 is lower than previously found (V. Kokorev et al. 2023), it still requires a heavy seed (i.e. $M_{\rm seed} > 10^3\,{\rm M}_\odot$) at high redshift, assuming constant Eddington-limited accretion. Of course, a constant Eddington-limited accretion over nearly 600 Myr is not physical. The actual mass accretion rate will likely vary over time, with both sub- and super-Eddington periods (e.g. L.-X. Li 2012; R. Schneider et al. 2023; A. Trinca et al. 2024; H. Hu et al. 2025). Simulations present a range of such accretion rates, with some showing that super-Eddington accretion could be sustained for up to tens of Myr (e.g. A. Lupi et al. 2024; L. R. Prole et al. 2025). But our constraint on the current Eddington ratio of UNCOVER_20466 does not allow us to comment on the past accretion.

Regardless, the high black hole mass of UNCOVER_20466 and similar high-redshift AGN are more easily explained if they evolved from a heavy seed. The high mass could also be explained by a primordial black holes (PBHs), which models predict to feature high masses ($\gtrsim 10^3\,{\rm M}_\odot$ at $z\sim 25$; e.g. P. Dayal 2024; B. Zhang, W.-X. Feng & H. An 2025; S. Zhang et al. 2025; F. Ziparo, S. Gallerani & A. Ferrara 2025).

The future evolutionary track of UNCOVER_20466 is non-trivial to determine, as we only have a constraint on the mass of the black hole and limits on the stellar and warm dust components. If there is a reservoir of molecular gas, then one possibility is that the black hole accretion remains low (as evidenced by the low $\lambda_{\rm Edd}$), while the gas is turned into stars. This would allow UNCOVER_20466 to stay on the $M_{\rm BH}-M_{\rm dyn}$ and $M_{\rm BH}-\sigma_*$ relations of Fig. 5 c and 5b, while moving closer to the $M_{\rm BH}-M_*$ relation of Fig. 5(a). However, the gas reservoir of this galaxy is not yet explored, and future ALMA observations are required. We note that the non-detection of [CII] or FIR emission in some LRDs (M. Xiao et al. 2025) suggests a small molecular gas reservoir. Alternatively, this system may have a substantial dark matter contribution, and later baryonic accretion may bring it closer to the local $M_{\rm BH}-M_*$ relation (W. McClymont et al. 2026).

However, the current black hole accretion rate is non-zero (i.e. $\lambda_{\rm Edd}\sim 0.1$), so the black hole mass will increase with cosmic time. One extreme possibility is shown by the dotted line of Fig. 6, which shows how $M_{\rm BH}$ would change with Eddington-limited accretion. This curve extends into the high-mass region of $z>7$ QSOs (X. Fan et al. 2023), but a more physical sub-Eddington (or variable) growth would result in a lower mass, more similar to other observed LRDs at $z\sim 6-8$.

Together, we find that UNCOVER_20466 likely evolved from a heavy seed at high redshift, featured strong AGN activity in the past, and at will either evolve by $z\sim 6$ into a source similar to LRDs (assuming low or negligible black hole growth) or QSOs (assuming a high growth rate). Recent studies have found a sample of $z<4$ galaxies with red inner regions and blue star-forming outskirts, either representing descendants of LRDs that have gained a blue envelope over time (J.-B. Billand et al. 2025) or showing that LRDs may already have faint star-forming regions that are simply not detectable at high redshift (P. Rinaldi et al. 2025a). This represents a possible picture of UNCOVER_20466, but there are several questions that are not yet answered. First, we cannot yet constrain the formation mechanism for the ionized bubble (see discussion of S. Fujimoto et al. 2024) that results in a high Lyα escape fraction and equivalent width. This could be caused by significant UV emission from young stars in the past, or by AGN activity (e.g. J. Witstok et al. 2024; D. Jiang et al. 2025). In addition, the dust geometry in the host galaxy and around the central black hole is not constrained. We also note the extremely large [OIII]λ4363/[OIII]λ5007 ratio suggests either abnormally high density or temperature. UNCOVER_20466 represents one of the most extreme sources at high redshift, and requires additional observations to further constrain its properties (e.g. with ALMA to constrain gas properties or *JWST*/NIRSpec G140M/F070LP to spectrally resolve the Lyα emission).

6 CONCLUSIONS

In this work, we presented new *JWST*/NIRSpec IFU data of the $z=8.50$ source UNCOVER_20466, taken as part of the BlackTHUNDER survey. While this source is spatially compact ($R_{\rm e}\lesssim$ 200 pc), our data enable accurate spectral extraction using a PSF-defined aperture loss correction verified by comparison with JWST/NIRCam photometry. By extracting integrated spectra of both the PRISM/CLEAR and G395H/F290LP data cubes and fitting each, we are able to measure continuum and line properties, yielding constraints on the properties of this source.

(i) We confirm the LRD status of UNCOVER_20466, with a v-shaped continuum ($\beta_{\rm UV}=-0.7\pm0.1$, $\alpha_{\rm opt}=1.8\pm0.2$) and compact morphology ($r_{\rm e}=0.18\pm0.06$ kpc, based on fits to NIRCam images). Similarly to many other LRDs, this source features broad Balmer emission (FWHM $=2503\pm176\,{\rm km\,s^{-1}}$) and is FIR-faint (e.g. C. M. Casey et al. 2025; S. Fujimoto et al. 2025).

(ii) The best-fit Balmer decrements are in agreement with the intrinsic values, which suggests a lack significant dust attenuation. The previous detection of higher attenuation ($A_{\rm V}\sim 2$; V. Kokorev et al. 2023) is discussed, including possible reasons for the disagreement with our fiducial values of $A_{\rm V}\sim 0$.

(iii) The broad Hβ emission and underlying continuum was used to constrain the black hole properties ($M_{\rm BH}\sim 10^{7.5-7.6}\,{\rm M}_\odot$, $\lambda_{\rm Edd}\sim 10$ per cent), which are slightly lower than previous estimates ($<2\sigma$ discrepant). Using an upper limit on M_* from literature, we confirm that UNCOVER_20466 features an overmassive black hole.

(iv) Our observed line ratios are combined with empirical relations and PYNEB to explore the properties of the host galaxy or gaseous envelope. We find a low [OII]λ3727/[OII]λ3729 ratio and a high [O III]λ4363/[O III]λ5007 ratio, which could be explained by a multiphase ISM (i.e. diffuse gas and dense gas) or an exceptionally high temperature ($T_{\rm e}\gtrsim 10^5$ K). Other line ratios reveal a low gas-phase metallicity of 0.12 ± 0.02 solar (from high-redshift line ratio calibrations of SFGs, with a higher value from AGN diagnostics) and a high ionization parameter of $\log_{10}(U)=-1.3\pm0.3$. While the applicability of these relations to high-redshift LRDs is not proven, this high temperature, high-ionization, extreme environment aligns with the compact AGN nature of this source.

(v) By leveraging an extensive grid of photoionization models, we have found that the extremely high [O III]λ4363/Hγ ratio indicates that the gas in the host galaxy is not only ionized and overheated by the AGN, but it also requires extremely high densities, of about 10^7 cm^{-3}. Together with the very high redshift at which this object is found (being one of the most distant LRDs), this finding is suggestive of a black hole that is forming in an ultra-dense protogalaxy in the early Universe.

(vi) Lyα emission is significantly detected, and is used to estimate an escape fraction of $f_{\rm esc}^{\rm Ly\alpha} \sim 30$ per cent. This places UNCOVER_20466 on existing correlations of $EW_{0,{\rm Ly}\alpha}$-$f_{\rm esc}^{\rm Ly\alpha}$ and $EW_{0,{\rm Ly}\alpha}$-$M_{\rm UV}$.

(vii) While UNCOVER_20466 features an overmassive black hole, we find that it lies on local correlations of $M_{\rm BH} - \sigma_*$ and $M_{\rm BH} - M_{\rm dyn}$. Since these correlations were primarily determined using the properties of local bulges, the observable emission of UNCOVER_20466 may represent the progenitor of the central bulge of a lower-redshift galaxy.

(viii) We compare the black hole mass of UNCOVER_20466 to other $z > 6$ AGN. While our new $M_{\rm BH}$ is lower than previous estimates, we find that it is still one of the highest-redshift and most massive black holes. Using a set of growth tracks assuming Eddington-limited accretion, we show that this source would likely require a heavy seed ($M_{\rm seed} \gtrsim 10^3$ assuming $z_{\rm seed} \sim 25$).

(ix) The combination of properties is synthesized to predict the history and future evolution of this source. One possibility is that UNCOVER_20466 underwent a period of rapid black hole accretion in the recent past (which increased $M_{\rm BH}$ and σ_* of the host galaxy) which has now ended (as evidenced by the low $\lambda_{\rm Edd}$). Depending on future accretion, it may evolve into a black hole similar to those of QSOs (high accretion) or LRDs (negligible accretion) at $z \sim 6$.

Our data show that UNCOVER_20466 is an exceptional source in the early Universe, with typical LRD properties, an overmassive black hole, evidence for a large ionized bubble, and extreme ISM conditions. Additional observations at different wavelengths (e.g. *JWST*/MIRI, ALMA [CII]158μm) will help to reveal the complex nature of this source.

ACKNOWLEDGEMENTS

We thank the anonymous referee for constructive feedback that has enhanced this work. GCJ, RM, XJ, FDE, IJ, and JS acknowledge support by the Science and Technology Facilities Council (STFC), by the ERC through Advanced Grant 695671 'QUENCH', and by the UKRI Frontier Research grant RISEandFALL. HÜ and GM acknowledge funding by the European Union (ERC APEX, 101164796). Views and opinions expressed are however those of the authors only and do not necessarily reflect those of the European Union or the European Research Council Executive Agency. Neither the European Union nor the granting authority can be held responsible for them. RM also acknowledges funding from a research professorship from the Royal Society. AJB acknowledges funding from the 'FirstGalaxies' Advanced Grant from the European Research Council (ERC) under the European Union's Horizon 2020 research and innovation programme (Grant agreement no. 789056). GC acknowledges support from the INAF GO grant 2024 'A JWST/MIRI MIRACLE: MidIR Activity of Circumnuclear Line Emission'. KI acknowledges support from the National Natural Science Foundation of China (12233001), the National Key R&D Program of China (2022YFF0503401), and the China Manned Space Program (CMS-CSST- 2025-A09). PGP-G and MP acknowledge support from grants PID2022-139567NB-I00, PID2024-159902NA-I00, and RYC2023-044853-I funded by Spanish Ministerio de Ciencia e Innovación MCIN/AEI/10.13039/501100011033, FEDER *Una manera de hacer Europa*, and El Fondo Social Europeo Plus FSE + . RS acknowledges support from the PRIN 2022 MUR project 2022CB3PJ3 – First Light And Galaxy aSsembly (FLAGS) funded by the European Union – Next Generation EU, and from EU-Recovery Fund PNRR – National Centre for HPC, Big Data, and Quantum Computing. ST acknowledges support by the Royal Society Research Grant G125142. This work is based in part on observations made with the NASA/ESA/CSA *JWST*. The data were obtained from the Mikulski Archive for Space Telescopes at the Space Telescope Science Institute, which is operated by the Association of Universities for Research in Astronomy, Inc., under NASA contract NAS 5–03127 for *JWST*.

DATA AVAILABILITY

The NIRSpec data used in this research was obtained within the NIRSpec-IFU GO programme 'Unveiling the nature and impact of the first population of black holes: an extensive NIRSpec-IFU survey in the first billion years' (PID 5015; https://doi.org/10.17909/m9xt-6908) and is publicly available. Data presented in this work will be shared upon reasonable request to the corresponding author.

REFERENCES

Abuter R. et al., 2024, Nature, 627, 281
Akins H. B. et al., 2025a, ApJ, 980, L29
Akins H. B. et al., 2025b, ApJ, 991, 37
Ananna T. T., Bogdán Á., Kovács O. E., Natarajan P., Hickox R. C., 2024, ApJ, 969, L18
Arribas S. et al., 2024, A&A, 688, A146
Baggen J. F. W. et al., 2024, ApJ, 977, L13
Baldwin J. A., Phillips M. M., Terlevich R., 1981, PASP, 93, 5
Baskin A., Laor A., 2005, MNRAS, 358, 1043
Begelman M. C., Dexter J., 2026, ApJ, 996, 48
Begley R. et al., 2024, MNRAS, 527, 4040
Bennert V. N. et al., 2021, ApJ, 921, 36
Bezanson R. et al., 2018, ApJ, 858, 60
Bezanson R. et al., 2024, ApJ, 974, 92
Billand J.-B. et al., 2025, preprint (arXiv:2507.04011)
Bosman S. E. I. et al., 2025, preprint (arXiv:2511.02902)
Bradley L. et al., 2021, astropy/photutils: 1.1.0, Zenodo
Brazzini M., D'Eugenio F., Maiolino R., Juodžbalis I., Ji X., Scholtz J., Chang S.-J., 2025, MNRAS, 544, L167
Bunker A. J. et al., 2023, A&A, 677, A88
Bunker A. J. et al., 2024, A&A, 690, A288
Bushouse H. et al., 2025, JWST Calibration Pipeline. Zenodo
Byrne C. M., Stanway E. R., Eldridge J. J., McSwiney L., Townsend O. T., 2022, MNRAS, 512, 5329
Calzetti D., Armus L., Bohlin R. C., Kinney A. L., Koornneef J., Storchi-Bergmann T., 2000, ApJ, 533, 682
Cameron A. J. et al., 2023, A&A, 677, A115
Cameron A. J., Katz H., Witten C., Saxena A., Laporte N., Bunker A. J., 2024, MNRAS, 534, 523
Cappellari M. et al., 2006, MNRAS, 366, 1126
Carniani S. et al., 2019, MNRAS, 489, 3939
Carniani S. et al., 2024, Nature, 633, 318
Carranza-Escudero M. et al., 2025, ApJ, 989, L50
Casey C. M. et al., 2025, ApJ, 990, L61
Cataldi E. et al., 2025, A&A, 703, A208

Ceci M. et al., 2025, preprint (arXiv:2507.08077)
Chisholm J. et al., 2024, MNRAS, 534, 2633
Choustikov N., Stiskalek R., Saxena A., Katz H., Devriendt J., Slyz A., Sub-department of Astrophysics U. O. O., 2025, MNRAS, 537, 2273
Cullen F. et al., 2025, MNRAS, 540, 2176
Curti M., Mannucci F., Cresci G., Maiolino R., 2020, MNRAS, 491, 944
Curti M. et al., 2023, MNRAS, 518, 425
Curti M. et al., 2025, A&A, 697, A89
Curtis-Lake E. et al., 2023, Nat. Astron., 7, 622
de Graaff A. et al., 2024, A&A, 684, A87
de Graaff A. et al., 2025a, preprint (arXiv:2511.21820)
de Graaff A. et al., 2025b, A&A, 701, A168
D'Eugenio F. et al., 2024, Nat. Astron., 8, 1443
D'Eugenio F. et al., 2025a, preprint (arXiv:2503.11752)
D'Eugenio F. et al., 2025b, ApJS, 277, 4
D'Eugenio F. et al., 2026, MNRAS, 545, staf2117
Dayal P., 2024, A&A, 690, A182
Donnan C. T. et al., 2024, MNRAS, 533, 3222
Donnan C. T. et al., 2025, ApJ, 993, 224
Dors O. L., 2021, MNRAS, 507, 466
Dottorini D. et al., 2025, A&A, 698, A234
Dumont A. et al., 2025, A&A, 703, A54
Endsley R. et al., 2022, MNRAS, 517, 5642
Endsley R. et al., 2024, MNRAS, 533, 1111
Fabian A. C., 2012, ARA&A, 50, 455
Fan X., Bañados E., Simcoe R. A., 2023, ARA&A, 61, 373
Feng W.-X., Yu H.-B., Zhong Y.-M., 2025, preprint (arXiv:2506.17641)
Ferland G. J., 1993, Hazy, A Brief Introduction to Cloudy 84, University of Kentucky Department of Physics and Astronomy Internal Report
Ferland G. J. et al., 2017, RMxAA, 53, 385
Fruchter A. S., Hook R. N., 2002, PASP, 114, 144
Fu S. et al., 2025, preprint (arXiv:2512.02096)
Fujimoto S. et al., 2024, ApJ, 977, 250
Fujimoto S. et al., 2025, ApJS, 278, 45
Fuller S. et al., 2020, ApJ, 896, 156
Furtak L. J. et al., 2023a, MNRAS, 523, 4568
Furtak L. J. et al., 2023b, ApJ, 952, 142
Furtak L. J. et al., 2024, Nature, 628, 57
Furtak L. J. et al., 2025, A&A, 698, A227
Ginolfi M. et al., 2020, A&A, 633, A90
Golubchik M. et al., 2025, preprint (arXiv:2512.02117)
Goovaerts I., Thai T. T., Pello R., Tuan-Anh P., Laporte N., Matthee J., Nanayakkara T., Pharo J., 2024, A&A, 690, A302
Gordon K. D., Clayton G. C., Misselt K. A., Landolt A. U., Wolff M. J., 2003, ApJ, 594, 279
Goulding A. D. et al., 2023, ApJ, 955, L24
Greene J. E., Ho L. C., 2005, ApJ, 630, 122
Greene J. E., Strader J., Ho L. C., 2020, ARA&A, 58, 257
Greene J. E. et al., 2024, ApJ, 964, 39
Hainline K. N. et al., 2024, ApJ, 975, 31
Hainline K. N. et al., 2025, ApJ, 979, 138
Harikane Y. et al., 2023, ApJ, 959, 39
Harikane Y. et al., 2025, ApJ, 993, 204
Heintz K. E. et al., 2024, Science, 384, 890
Hoag A. et al., 2019, ApJ, 878, 12
Hu H., Inayoshi K., Haiman Z., Ho L. C., Ohsuga K., 2025, ApJ, 983, L37
Husemann B., Wisotzki L., Sánchez S. F., Jahnke K., 2013, A&A, 549, A43
Husemann B., Jahnke K., Sánchez S. F., Wisotzki L., Nugroho D., Kupko D., Schramm M., 2014, MNRAS, 443, 755
Hviding R. E. et al., 2025, A&A, 702, A57
Inayoshi K., 2025, ApJ, 988, L22
Inayoshi K., Shangguan J., Chen X., Ho L. C., Haiman Z., 2025, preprint (arXiv:2505.05322)
Isobe Y., Ouchi M., Nakajima K., Harikane Y., Ono Y., Xu Y., Zhang Y., Umeda H., 2023, ApJ, 956, 139
Isobe Y. et al., 2025, MNRAS, 541, L71
Izotov Y. I., Schaerer D., Worseck G., Verhamme A., Guseva N. G., Thuan T. X., Orlitová I., Fricke K. J., 2020, MNRAS, 491, 468
Ji X. et al., 2024, MNRAS, 535, 881
Ji X. et al., 2025a, MNRAS, 541, 2134
Ji X. et al., 2025b, MNRAS, 544, 3900
Jiang D., Jiang L., Sun S., Liu W., Fu S., 2025, Nat. Astron., 9, 1890
Jockel C., Kawaguchi K., Fujibayashi S., Shibata M., 2026, MNRAS, 545, staf1949
Jones G. C. et al., 2024a, preprint (arXiv:2412.15027)
Jones G. C. et al., 2024b, A&A, 683, A238
Jones G. C. et al., 2025a, MNRAS, 536, 2355
Jones G. C. et al., 2025b, MNRAS, 540, 3311
Jung I. et al., 2022, preprint (arXiv:2212.09850)
Juodžbalis I. et al., 2024, Nature, 636, 594
Juodžbalis I. et al., 2025a, preprint (arXiv:2504.03551)
Juodžbalis I. et al., 2025b, preprint (arXiv:2508.21748)
Kageura Y. et al., 2025, ApJS, 278, 33
Katz H. et al., 2023, MNRAS, 518, 592
Kido D., Ioka K., Hotokezaka K., Inayoshi K., Irwin C. M., 2025, MNRAS, 544, 3407
Kiyota T. et al., 2025, ApJ, 995, 150
Kocevski D. D. et al., 2023, ApJ, 954, L4
Kocevski D. D. et al., 2025, ApJ, 986, 126
Kokorev V. et al., 2023, ApJ, 957, L7
Kokorev V. et al., 2024, ApJ, 968, 38
Kormendy J., Ho L. C., 2013, ARA&A, 51, 511
Kroupa P., 2001, MNRAS, 322, 231
Kuruvanthodi A., Schaerer D., Marques-Chaves R., Korber D., Weibel A., Oesch P. A., Roberts-Borsani G., 2024, A&A, 691, A310
Labbe I. et al., 2025, ApJ, 978, 92
Lambrides E. et al., 2025, preprint (arXiv:2509.09607)
Langeroodi D., Hjorth J., 2023, ApJ, 957, L27
Larson R. L. et al., 2023, ApJ, 953, L29
Laseter I. H. et al., 2024, A&A, 681, A70
Leung G. C. K. et al., 2025, ApJ, 992, 26
Li L.-X., 2012, MNRAS, 424, 1461
Li S. et al., 2025, ApJ, 979, L13
Li Z., Inayoshi K., Chen K., Ichikawa K., Ho L. C., 2025, ApJ, 980, 36
Lin X. et al., 2025, preprint (arXiv:2507.10659)
Liu H., Jiang Y.-F., Quataert E., Greene J. E., Ma Y., 2025, ApJ, 994, 113
Lupi A., Quadri G., Volonteri M., Colpi M., Regan J. A., 2024, A&A, 686, A256
Luridiana V., Morisset C., Shaw R. A., 2015, A&A, 573, A42
Maiolino R. et al., 2024, A&A, 691, A145
Maiolino R. et al., 2025a, preprint (arXiv:2505.22567)
Maiolino R. et al., 2025b, MNRAS, 538, 1921
Marconcini C. et al., 2024, MNRAS, 533, 2488
Marconi A. et al., 2024, A&A, 689, A78
Marshall M. A. et al., 2023, A&A, 678, A191
Marshall M. A. et al., 2025a, A&A, 702, A50
Marshall M. A. et al., 2025b, A&A, 702, A174
Mascia S. et al., 2023, A&A, 672, A155
Matthee J. et al., 2024, ApJ, 963, 129
Mazzolari G. et al., 2024, A&A, 691, A345
Mazzolari G. et al., 2025, A&A, 700, A12
McClymont W. et al., 2025, MNRAS, 540, 190
McClymont W. et al., 2026, MNRAS, 545, staf2092
Morisset C. et al., 2016, A&A, 594, A37
Naidu R. P. et al., 2025a, preprint (arXiv:2503.16596)
Naidu R. P. et al., 2025b, preprint (arXiv:2505.11263)
Nakajima K., Ouchi M., 2014, MNRAS, 442, 900
Nakajima K., Ouchi M., Isobe Y., Harikane Y., Zhang Y., Ono Y., Umeda H., Oguri M., 2023, ApJS, 269, 33
Nandal D., Loeb A., 2025, preprint (arXiv:2507.12618)
Napolitano L. et al., 2024, A&A, 688, A106
Napolitano L. et al., 2025, ApJ, 989, 75
Natarajan P., Pacucci F., Ricarte A., Bogdán Á., Goulding A. D., Cappelluti N., 2024, ApJ, 960, L1

Newville M., Stensitzki T., Allen D. B., Ingargiola A., 2014, LMFIT: Non-Linear Least-Square Minimization and Curve-Fitting for Python. Zenodo
Ono Y. et al., 2012, ApJ, 744, 83
Onoue M. et al., 2025, Nat. Astron., 9, 1541
Orozco E. A., Jiménez-Andrade E. F., Murphy E. J., Smail I., Momjian E., Heywood I., Vega-Gutierrez M., DeCoursey C., 2025, preprint (arXiv:2506.20634)
Pasha I., Miller T. B., 2023, The Journal of Open Source Software, 8, 5703
Pentericci L. et al., 2018, A&A, 619, A147
Pérez-González P. G. et al., 2025, Nat. Astron., 9, 1240
Perna M. et al., 2023, A&A, 679, A89
Perrin M. D., Long J., Sivaramakrishnan A., Lajoie C.-P., Elliot E., Pueyo L., Albert L., 2015, Astrophysics Source Code Library, record ascl:1504.007
Pirzkal N. et al., 2024, ApJ, 969, 90
Pollock C. L. et al., 2025, preprint (arXiv:2506.15779)
Price S. H. et al., 2025, ApJ, 982, 51
Prieto-Jiménez C. et al., 2025, A&A, 701, A31
Prole L. R. et al., 2025, preprint (arXiv:2511.09640)
Reines A. E., Volonteri M., 2015, ApJ, 813, 82
Rinaldi P. et al., 2025a, preprint (arXiv:2507.17738)
Rinaldi P. et al., 2025b, ApJ, 994, 86
Roberts M. G., Braff L., Garg A., Profumo S., Jeltema T., 2025, preprint (arXiv:2507.03230)
Robertson B. et al., 2024, ApJ, 970, 31
Rodriguez L. F., Mirabel I. F., 2025, preprint (arXiv:2512.03331)
Ronayne K. et al., 2025, preprint (arXiv:2508.20177)
Roy N. et al., 2023, ApJ, 952, L14
Rusakov V. et al., 2025, preprint (arXiv:2503.16595)
Sacchi A., Bogdán Á., 2025, ApJ, 989, L30
Sanders R. L., Shapley A. E., Topping M. W., Reddy N. A., Brammer G. B., 2024, ApJ, 962, 24
Saxena A. et al., 2024a, preprint (arXiv:2411.14532)
Saxena A. et al., 2024b, A&A, 684, A84
Scarlata C., Hayes M., Panagia N., Mehta V., Haardt F., Bagley M., 2024, preprint (arXiv:2404.09015)
Schaerer D., Marques-Chaves R., Barrufet L., Oesch P., Izotov Y. I., Naidu R., Guseva N. G., Brammer G., 2022, A&A, 665, L4
Schenker M. A., Stark D. P., Ellis R. S., Robertson B. E., Dunlop J. S., McLure R. J., Kneib J.-P., Richard J., 2012, ApJ, 744, 179
Schneider R., Valiante R., Trinca A., Graziani L., Volonteri M., Maiolino R., 2023, MNRAS, 526, 3250
Scholtz J. et al., 2024, A&A, 687, A283
Scholtz J. et al., 2025a, MNRAS, 545, staf2107
Scholtz J. et al., 2025b, MNRAS, 539, 2463
Setton D. J. et al., 2025a, ApJ, 991, L10
Setton D. J. et al., 2025b, ApJ, 995, 118
Shen Y. et al., 2015, ApJ, 805, 96
Shimizu S., Kashikawa N., Kikuta S., Takeda Y., Arita J., Emori R., Koretomo K., 2025, MNRAS, 542, 3125
Simmonds C. et al., 2024, MNRAS, 535, 2998
Song M., Finkelstein S. L., Livermore R. C., Capak P. L., Dickinson M., Fontana A., 2016, ApJ, 826, 113
Stanway E. R., Eldridge J. J., 2018, MNRAS, 479, 75
Stark D. P., Ellis R. S., Chiu K., Ouchi M., Bunker A., 2010, MNRAS, 408, 1628
Stern J., Laor A., 2012, MNRAS, 423, 600
Suess K. A. et al., 2024, ApJ, 976, 101
Sun B., Yan H., 2025, preprint (arXiv:2503.21896)
Tacchella S. et al., 2025, MNRAS, 540, 851
Tang M. et al., 2023, MNRAS, 526, 1657
Tang M., Stark D. P., Topping M. W., Mason C., Ellis R. S., 2024, ApJ, 975, 208
Tang M. et al., 2025, ApJ, 991, 217
Taylor A. J. et al., 2025, ApJ, 989, L7
Tilvi V. et al., 2020, ApJ, 891, L10
Topping M. W. et al., 2024a, MNRAS, 529, 3301
Topping M. W. et al., 2024b, MNRAS, 529, 4087
Trefoloni B. et al., 2025, A&A, 700, A203
Trinca A. et al., 2024, preprint (arXiv:2412.14248)
Tripodi R. et al., 2024, A&A, 692, A184
Tripodi R. et al., 2025, Nature Communications, 16, 9830
Übler H. et al., 2023, A&A, 677, A145
Übler H. et al., 2024, MNRAS, 531, 355
Usui M. et al., 2025, ApJ, 991, L38
van der Wel A. et al., 2022, ApJ, 936, 9
Vanzella E. et al., 2011, ApJ, 730, L35
Veilleux S., Osterbrock D. E., 1987, ApJS, 63, 295
Venturi G. et al., 2024, A&A, 691, A19
Vestergaard M., Peterson B. M., 2006, ApJ, 641, 689
Vikaeus A. et al., 2024, MNRAS, 529, 1299
Wang B. et al., 2024, ApJ, 969, L13
Wang B. et al., 2025, ApJ, 984, 121
Whitler L., Stark D. P., Mason C. A., Tang M., Chen Z., Lu T.-Y., Prieto-Lyon G., Hutter A., 2025a, preprint (arXiv:2510.12019)
Whitler L. et al., 2025b, ApJ, 992, 63
Willott C. J. et al., 2025, ApJ, 988, 26
Witstok J., Jones G. C., Maiolino R., Smit R., Schneider R., 2023, MNRAS, 523, 3119
Witstok J. et al., 2024, A&A, 682, A40
Witstok J. et al., 2025, Nature, 639, 897
Xiao M. et al., 2025, A&A, 700, A231
Yang H. et al., 2017, ApJ, 844, 171
Yeh S. C. C., Matzner C. D., 2012, ApJ, 757, 108
Yue M., Eilers A.-C., Ananna T. T., Panagiotou C., Kara E., Miyaji T., 2024, ApJ, 974, L26
Zamora S. et al., 2025a, preprint (arXiv:2512.09022)
Zamora S. et al., 2025b, A&A, 702, A102
Zhang B., Feng W.-X., An H., 2025, preprint (arXiv:2507.07171)
Zhang H., Behroozi P., Volonteri M., Silk J., Fan X., Hopkins P. F., Yang J., Aird J., 2023, MNRAS, 518, 2123
Zhang H. et al., 2025, MNRAS, 538, 503
Zhang J. et al., 2025, preprint (arXiv:2505.02895)
Zhang S., Liu B., Bromm V., Kühnel F., 2025, preprint (arXiv:2512.14066)
Zhang Y. et al., 2025, preprint (arXiv:2510.25830)
Zhu P., Kewley L. J., Sutherland R. S., 2024, ApJ, 977, 187
Ziparo F., Gallerani S., Ferrara A., 2025, J. Cosmol. Astropart. Phys., 2025, 040

APPENDIX A: IFU-MSA SPECTRAL COMPARISON

As part of our analysis of the *JWST*/NIRSpec IFU observations of UNCOVER_20466, we compare the best-fitting properties to the JWST/NIRSpec MSA observations of this source as presented by V. Kokorev et al. (2023). While many properties are the same (e.g. redshift, presence of broad Hβ and an overmassive black hole), some line fluxes are significantly different (up to a factor of ~ 2; see Table 2). Here, we investigate the origin of this discrepancy.

First, we consider differences in the studied spectra, through extraction method or aperture/slit loss correction. The calibrated UNCOVER MSA spectrum (S. H. Price et al. 2025; available from the survey website[10]) is compared to our extracted IFU spectrum (with aperture loss correction) in Fig. A1. While the two spectra feature small differences, there are no large-scale or wavelength-dependent differences between them.

Instead, we consider our treatment of the NIRSpec LSF. While we use the fiducial LSF directly, V. Kokorev et al. (2023) assume $\mathrm{LSF}/\mathrm{LSF}_{\mathrm{fiducial}} = 0.59$ (A. de Graaff et al. 2024). If we instead adopt this narrower LSF, then we find slightly smaller intrinsic

[10] https://jwst-uncover.github.io/DR4.html

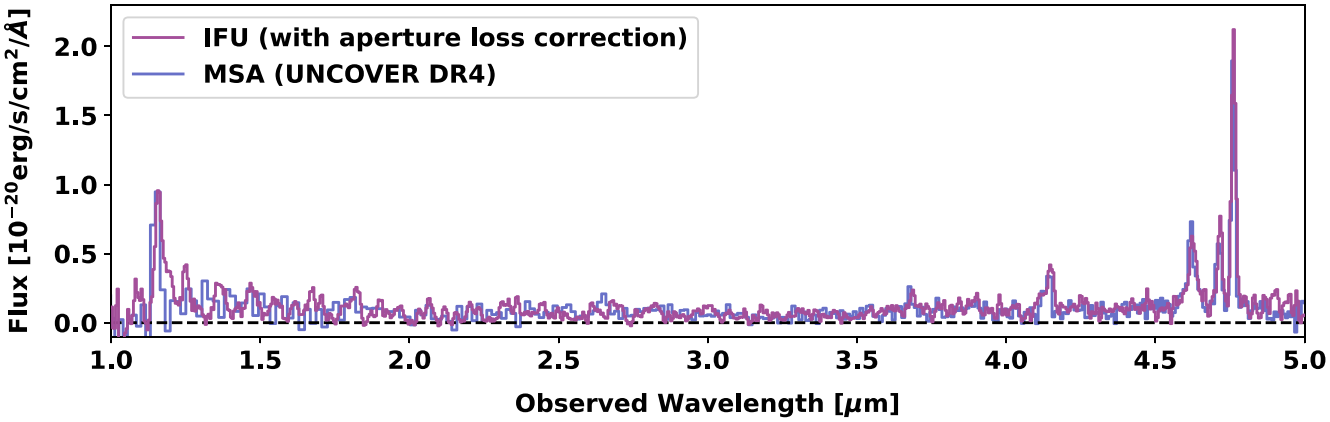

Figure A1. UNCOVER_20466 spectra from this work (pink) compared to NIRSpec MSA observations (S. H. Price et al. 2025, blue). All data have been corrected for gravitational magnification and slit or aperture loss.

linewidths and larger fluxes for some lines (but still not in agreement with the values of V. Kokorev et al. 2023). If we allow the deviation from the LSF to vary, then we find a best-fit value of $\mathrm{LSF/LSF_{fiducial}} = 0.89$ and similar line fluxes as the fiducial case. Therefore, we do not consider the LSF treatment to be responsible for the discrepancy with previous results, and adopt the fiducial value in our analysis.

As a final test, we consider the possibility that our use of a Gaussian profile is to blame for the discrepancy in fluxes. We estimate a non-parametric total flux of [OIII]λ5007 by isolating the spectral range around this line ($4.73 < \lambda_{\mathrm{obs}}/\mu\mathrm{m} < 4.78$), subtracting the best-fit continuum flux, and integrating the IFU spectra—resulting in a slightly lower value than the best-fit integrated flux (324×10^{-20} erg s^{-1} cm^{-2} versus $\sim 360 \times 10^{-20}$ erg s^{-1} cm^{-2} in Table 2).

These tests show that the UNCOVER NIRSpec MSA spectrum agrees with the NIRSpec IFU spectrum studied here, and that the higher fluxes in a previous work are not due to the assumed LSF or assumed line shape. Both spectra were corrected by the same gravitational magnification, and comparisons to NIRCam data have confirmed that their slit or aperture loss corrections are valid. While the discrepancy may be caused by a combination of multiple effects, we note that due to the conservative uncertainties presented by V. Kokorev et al. (2023), the redshift, FWHMs and most line fluxes agree to within 3σ (e.g. Lyα, [O II]λλ3727, 3729, [NeIII]λ3869).

APPENDIX B: JWST/NIRCAM FILTERS

UNCOVER_20466 benefits from a wealth of JWST/NIRCam imaging from two programmes (see Section 2.2). We use a subset of these images to test the flux calibration of our data (Section D4), and to extract morphological properties of UNCOVER_20466 (Section 4.6). The filters of use are listed in Table B1, along with their programme of origin, pivot wavelength[11], and empirical PSF FWHM[12] in Table B1.

[11] Pivot wavelength taken from JDOX: https://jwst-docs.stsci.edu/jwst-near-infrared-camera/nircam-instrumentation/nircam-filters

[12] NIRSpec PSFs taken from JDOX: https://jwst-docs.stsci.edu/jwst-near-infrared-camera/nircam-performance/nircam-point-spread-functions

Table B1. Details of JWST/NIRCam filters used in this work.

Filter	PID	λ_{pivot} (μm)	$\mathrm{FWHM_{PSF,emp}}$ (arcsec)
F335M	4111	3.362	0.111
F356W[a]	2561	3.565	0.116
F360M	4111	3.623	0.120
F410M[a]	2561	4.083	0.137
F430M	4111	4.281	0.144
F444W[a]	2561	4.402	0.145
F460M[a]	4111	4.630	0.157
F480M[a]	4111	4.817	0.164

[a] Fit with pysersic to find morphological properties (Section 4.6).

APPENDIX C: SERENDIPITOUS SOURCE

Despite the small field of view of our NIRSpec IFU data (~ 3.6 arcsec $\times$ 3.8 arcsec due to dithering and drizzling), we also find a serendipitous line-emitting source which we name 'BlackBolt-1' (inspired by the theme of 'BlackTHUNDER'). This source lies on the edge of the field of view, ~ 2.2 arcsec to the north-west of UNCOVER_20466 (i.e. at 00:14:33.614 -30:23:09.4467). This location places it within 0.2 arcsec of an object in the 'Medium Bands, Mega Science' data release[13] (ID 21646; K. A. Suess et al. 2024) which has $z_{\mathrm{phot}} = 6.68^{+0.03}_{-0.04}$ based on the JWST/NIRCam photometry.

Because of its location, we are not currently able to present a well-calibrated spectrum (i.e. some data are excluded due to high noise levels, and the PSF is not well determined at the edge of the field of view). However, we are able to define an aperture by performing a 2-D Gaussian fit to the emission of the brightest spectral channel and taking the resulting best-fitting major axis FWHM (0.2 arcsec). By extracting a spectrum from the R100 cube centred on this location using a circular aperture of radius 0.2 arcsec, we may determine its spectroscopic redshift.

As seen in Fig. C1, BlackBolt-1 features at least four strong line detections, all at different observed wavelengths than the lines detected from UNCOVER_20466 (i.e. this is not a lensed image). We use these lines to identify the redshift to be $z_{\mathrm{spec}} = 5.511$, based on the identification of the [O III]-Hβ complex and Hα, as well as the Lyα break.

[13] https://jwst-uncover.github.io/DR3.html

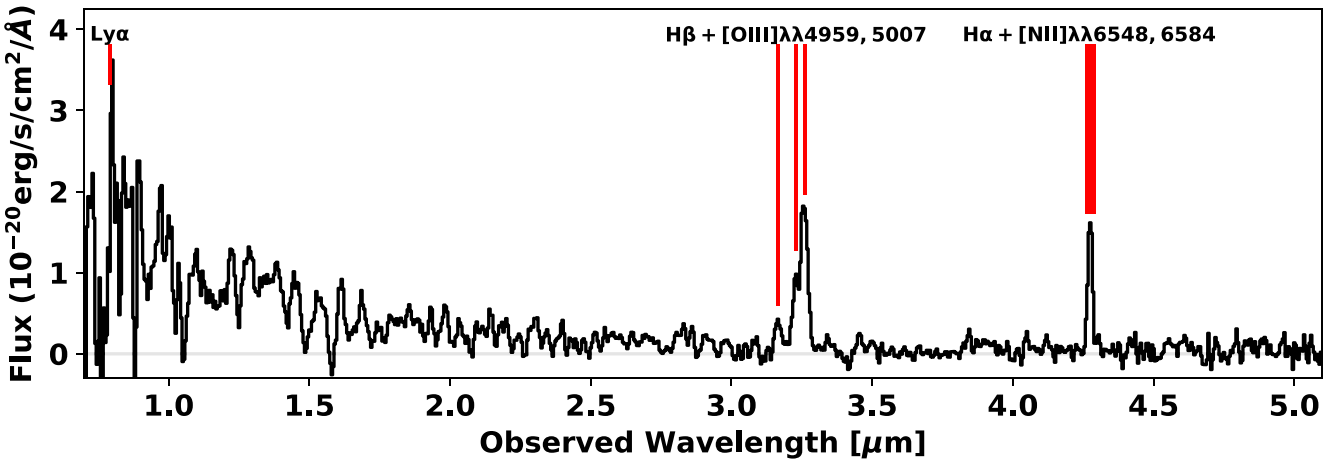

Figure C1. Integrated spectrum for a serendipitous source identified within the field of view (BlackBolt-1), extracted from 00:14:33.614 -30:23:09.4467 using a circular aperture of radius 0.2 arcsec from the R100 cube. No corrections have been applied, and the line fluxes are affected by noise artifacts due to its location on the edge of the data cube. Despite this, we identify the spectroscopic redshift of $z_{\rm spec} = 5.511$ based on several line detections (red lines).

Since this source is at a much lower redshift than our target, it is observed at a very different epoch (i.e. ~ 1.0 Gyr after the Big Bang, rather than ~ 0.58 Gyr for UNCOVER_20466). With this in mind, we do not include BlackBolt-1 in our analysis, but note that further analysis may be performed in a future work.

APPENDIX D: DETAILS OF APERTURE LOSS CORRECTION

When analysing the integrated spectra of UNCOVER_20466, we choose an extraction aperture of radius $0.125''$ in order to maximize the S/N of [OIII]λ5007. This aperture captures most of the emission from this compact object, but some emission from the wings of the PSF is missed. This fraction of missed flux is not constant, as the NIRSpec IFU PSF size changes with wavelength. In order to recover the total flux, an aperture loss correction is required (see similar analyses for NIRSpec IFU data in S. Arribas et al. 2024; S. Zamora et al. 2025b). In this Appendix, we detail how we calculate wavelength-dependent aperture loss corrections for our extracted spectra.

D1 NIRSpec IFU PSF derivation

We begin by analysing the shape of the NIRSpec IFU PSF. An in-depth characterization of the NIRSpec PSF was performed by F. D'Eugenio et al. (2024). This work found a strong evolution of the PSF FWHM with wavelength, as well as a significant difference in the PSF width across and along the NIRSpec slice directions (up to ~ 40 per cent). Although three approaches were utilized, no concrete PSF shape was found. The results of this work were adopted by many other NIRSpec/IFU studies (e.g. C. Marconcini et al. 2024; G. Venturi et al. 2024). To verify these results, we analyse archival observations of calibration stars, and compare the results to empirical models.

Observations of stars were included in programmes in order to calibrate the PSF of NIRSpec (PSFSTARUHSJ0439 in PID 1222, PI C. J. Willott; PSFSTARULASJ1342 in PID 1219, PI N. Luetzgendorf). Additionally, we consider the calibration data of PID 1537 (PI: K. D. Gordon), who observed the white dwarf G191-B2B with the JWST/NIRSpec IFU with all three R1000 gratings and all three R2700 gratings. For all of these observations, we downloaded the calibrated (stage 3) data cubes from the MAST archive and fit the stellar emission in each spectral channel of each cube with a 2D Gaussian model. The geometric mean of the best-fit semi-major axes were recorded, resulting in curves of PSF FWHM as a function of wavelength.

The resulting curves are shown in Fig. D1. Because the data of G191-B2B features significant oscillations in FWHM ('wiggles', see M. Perna et al. 2023; A. Dumont et al. 2025), we fit a third-order polynomial to each of the curves for this source. PSFSTARULASJ1342 and PSFSTARUHSJ0439 show elevated flux between $\lambda_{\rm obs} \sim 1.0-1.5\,\mu$m. This may be due to saturation of the NIRSpec detector, which would result in a non-Gaussian source and thus an inflated FWHM. For comparison, we also display results from F. D'Eugenio et al. (2024) (methods II and III), and the FWHM values derived from QSO observations (M. A. Marshall et al. 2023, 2025b) using the code QDEBLEND3D (B. Husemann et al. 2013, 2014).

It is clear that the curves of F. D'Eugenio et al. (2024) fall beneath those of the calibration star observations. This could be due to the fact that the serendipitous source studied by F. D'Eugenio et al. (2024) fell on the edge of the field of view rather than the pointing centre. Indeed, their analysis of a separate stellar observation (Method I) resulted in a larger PSF, in better agreement with the stars studied here.

Finally, we compare all of our approaches to the empirical curve outputted by STPSF[14], the successor to WEBBPSF (M. D. Perrin et al. 2015). This code takes many properties of the NIRSpec instrument into account (e.g. geometric distortion, detector charge transfer effects), resulting in physical models of the wavelength dependence of the PSF. The resulting PSF FWHM curve is in agreement with the results of calibration star observations, so we will use this model (hereafter referred to as the fiducial PSF) for our analyses.

[14] https://stpsf.readthedocs.io/en/latest/

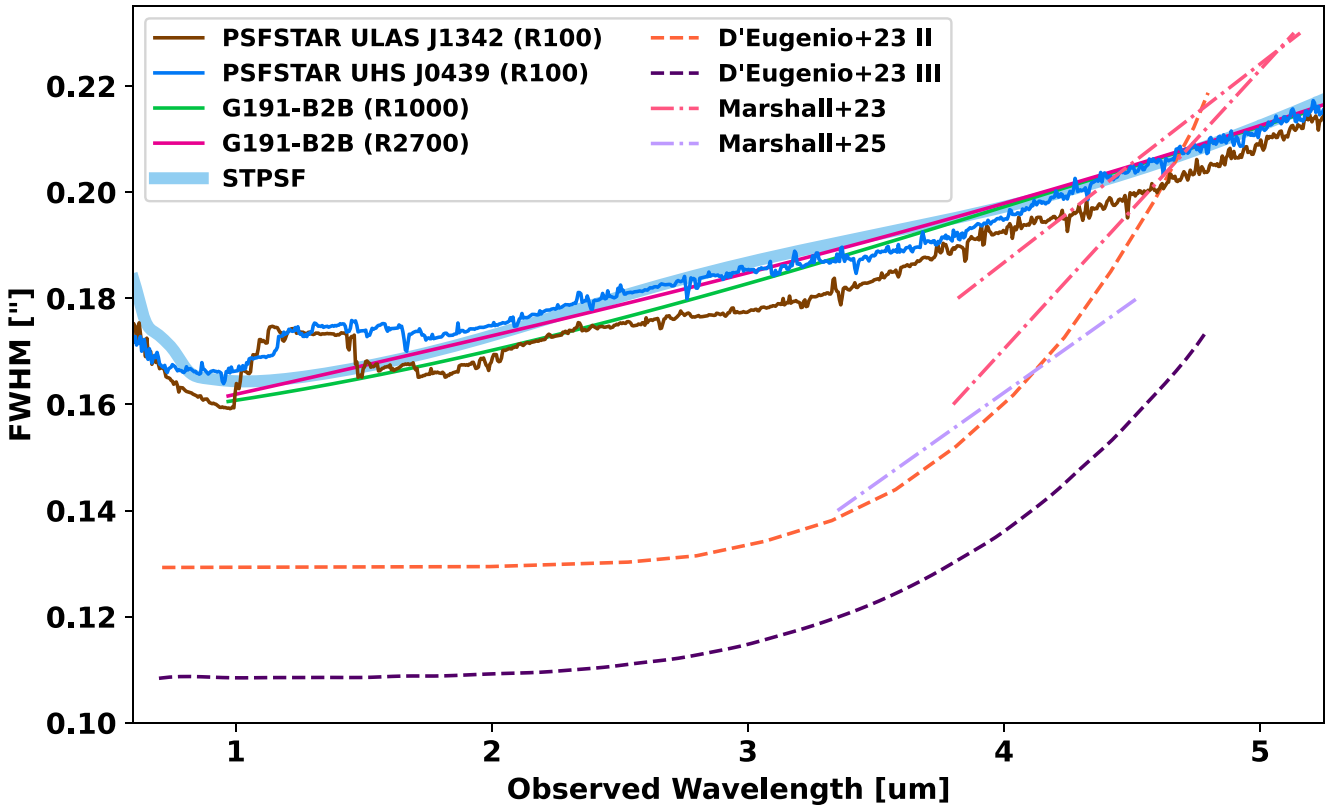

Figure D1. Best-fit FWHMs of the NIRSpec IFU PSF, derived using a variety of methods. Two methods of F. D'Eugenio et al. (2024) are shown by dashed lines, while the results of QDEBLEND3D fits to QSO observations are shown by dot–dashed lines (M. A. Marshall et al. 2023, 2025b). The FWHM curves derived from observations of three stars are shown by thin lines, while the empirical curve from STPSF is depicted with a thick line.

D2 Comparison with observed curve of growth

While this fiducial PSF is in good agreement with the shapes of observed point sources, we note that Appendix D1 and other works (e.g. F. D'Eugenio et al. 2024) used a two-dimensional Gaussian to model the PSF. In reality, the JWST/NIRSpec PSF is more complex, with a bright core and a fainter six-pointed 'snowflake' pattern of maxima and minima. While a 2D Gaussian model can describe the dominant central emission, the lower-level emission deviates from this axisymmetric model. We explore this by creating curves of growth (CoGs), which show the amount of flux contained within circular apertures of increasing radius. The slope of these CoGs are directly related to the density of flux: a bright core will result in a rapid rise, while diffuse emission will create a more shallow increase. We compare the CoGs for the observed [O III]λ5007 emission in the R100 and R2700 cubes, our best-fit 2D Gaussian model to the PSF, and the fiducial PSF.

To create the [O III]λ5007 CoG, we extracted spectra using circular apertures centred on UNCOVER_20466 with a range of radii ($0.025'' - 0.500''$), isolated the wavelength range around [O III]λ5007, fit the continuum and line emission in the resulting spectrum, and recorded the best-fit line flux for each aperture. The resulting CoGs are shown as red lines in Fig. D2. In order to create a similar CoG for the fiducial PSF of Section D1, we integrate the PSF within a range of apertures and normalize each flux to the value in the largest aperture ($r = 0.5$ arcsec; see magenta line with circular markers in Fig. D2). Finally, we create CoGs for 2D Gaussian models with the same FWHM as the fiducial model, assuming a circular model ($q = 1.0$) and an elongated model ($q = 0.5$).

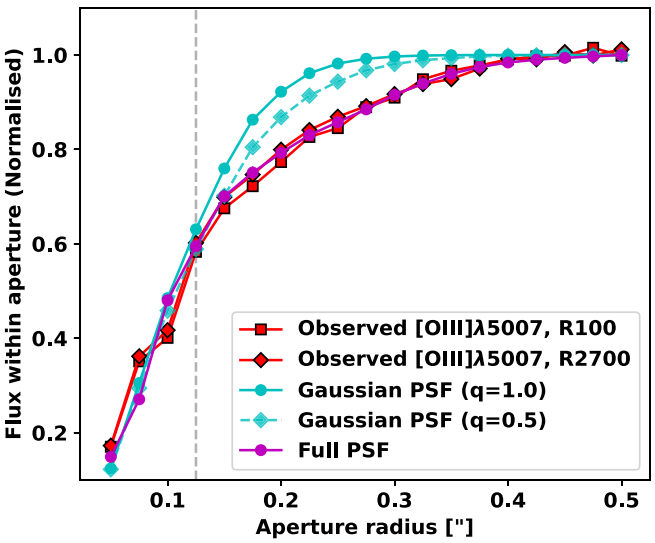

Figure D2. Curves of growth for our observations and models of the fiducial PSF. In red, we show the CoG for [O III]λ5007, as extracted from both observed cubes. The blue lines show the CoG of 2D Gaussian models, assuming different axis ratios (q). The purple line shows the CoG of the fiducial model.

From this analysis, we see that all of the CoGs agree at small radii ($r \lesssim 0.125$ arcsec) and large radii ($r \gtrsim 0.4$ arcsec), but the

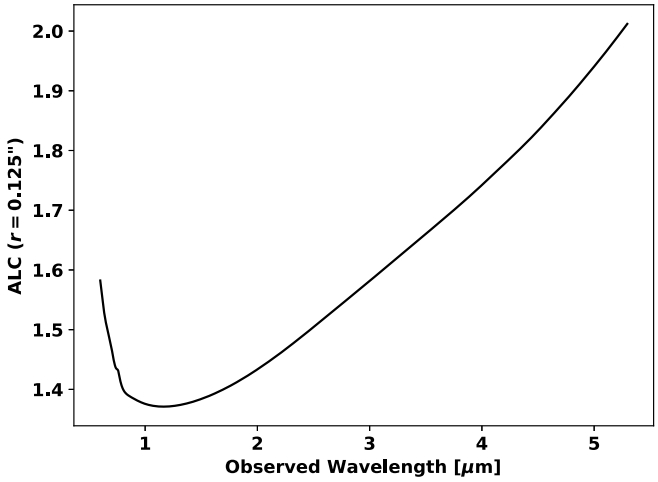

Figure D3. Aperture loss correction as function of observed wavelength for a circular aperture with radius 0.125″. This was derived using the full PSF model from STPSF, rather than a Gaussian approximation.

2D Gaussian model of the PSF deviates at intermediate radii ($0.125\,\mathrm{arcsec} \lesssim r \lesssim 0.400\,\mathrm{arcsec}$). This behaviour indicates diffuse emission in the PSF that is not present in the 2D Gaussian model. Because the full PSF follows the observed CoG more closely, we will use this fiducial PSF rather than a Gaussian approximation.

D3 Aperture loss correction

We have now characterized the wavelength-dependent FWHM of the NIRSpec IFU PSF, and tested this model on our observations. The remaining step is to derive the aperture loss correction curve for our adopted aperture ($r = 0.125\,\mathrm{arcsec}$). This is done by numerically integrating the full corresponding PSF and dividing by the value within the aperture. The resulting correction as a function of wavelength is shown in Fig. D3.

D4 Comparison to NIRCam data

While this empirical model is a good match to observations of stars, it is not yet thoroughly tested on observational data of high-redshift galaxies, and thus may not be accurate. To validate this correction, we conduct a comparison of our R100 NIRSpec spectrum and archival *JWST*/NIRCam photometry of UNCOVER_20466.

First, we extract fluxes from each NIRCam image by fitting each with a 2D circular Gaussian model with a constant offset (to account for background emission), where the FWHM of the model is set to be the fiducial FWHM from JDOX (see Table B1). In order to compare these photometric points to the NIRSpec data directly, we first convolve the R100 cube with the throughput curve of each NIRCam filter to create a set of pseudo-photometric images, and measure the flux using a circular aperture of $r = 0.125\,\mathrm{arcsec}$. We apply the aperture loss correction derived in Appendix D3 to the NIRSpec fluxes, and compare the resulting values in Fig. D4. We limit the comparison to NIRCam filters at $\lambda_{\mathrm{obs}} > 3\,\mu\mathrm{m}$ due to elevated noise on the blue side of the NIRSpec data. The resulting fluxes are comparable.

D5 Note on variability

By comparing *JWST*/NIRSpec MSA and IFU data taken at different times, X. Ji et al. (2025b) found that Abell2744-QSO1 featured significant variability. This analysis benefitted from the gravitationally lensed nature of the source: each of the three lensed images represented a different light travel time. Thus, they were able to show that Hβ rest-frame equivalent width decreased by ~ 50 per cent over an observer-frame time of $\sim 20\,\mathrm{yr}$.

While UNCOVER_20466 is not multiply lensed, it is possible that we could use the different data to explore the variability of this source. This is because of the different observation times: the NIRCam data were taken in two epochs (2 November 2022 for PID 2561, 11 November 2023 for PID 4111), while the *JWST*/NIRSpec MSA data were taken on 2023 July 31 and the JWST/NIRSpec IFU were taken on 5 December 2024. But as

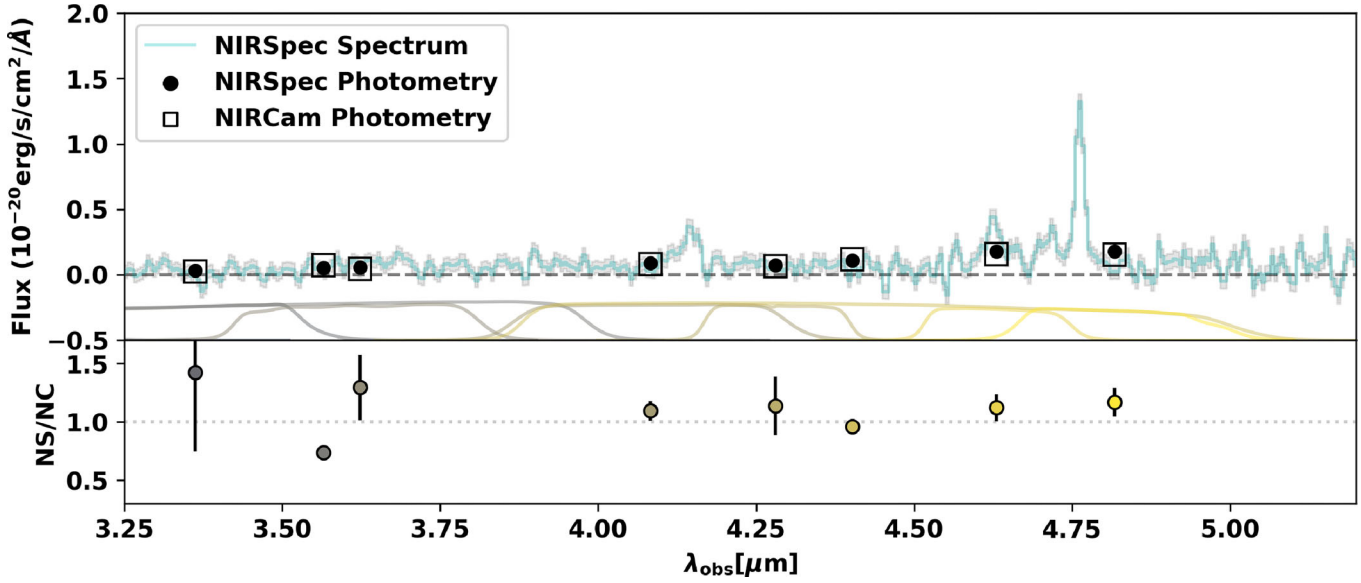

Figure D4. Comparison of the *JWST*/NIRSpec R100 spectrum and pseudo-photometry with *JWST*/NIRCam photometry (top panel). The pseudo-photometry was created using the throughput curves for each NIRCam fschoilter, shown in the lower portion of the top panel. This results in ratio of NIRSpec to NIRCam photometric fluxes that are in broad agreement with the expected value from the empirical NIRSpec PSF (lower panel).

demonstrated in Appendix D4, we find good agreement between the NIRCam data taken on each date and the IFU data, and thus no significant evidence for continuum variability on the observer-frame timescale of ~ 2 yr. In addition, the agreement between the MSA and IFU spectra (see Appendix A) suggests no significant change in emission line strength on an observer-frame timescale of ~ 1 yr.

APPENDIX E: LYMAN ALPHA CORRELATIONS

Ly α emission in galaxies appears to follow a few well-determined trends, where the Lyα equivalent width correlates with the Ly α escape fraction (e.g. R. Begley et al. 2024; I. Goovaerts et al. 2024), and with $M_{\rm UV}$ (e.g. G. C. Jones et al. 2024b, 2025a). However, much of this work has been done at lower redshift ($z < 8$). While LAEs have been discovered well into the epoch of reionization ($z > 10$; e.g. J. Witstok et al. 2025), the high redshift and LRD nature of UNCOVER_20466 make it an interesting source to examine in light of these correlations.

In Fig. E1, we show the placement of UNCOVER_20466 on two Ly α correlations, and compare it to a set of $z > 7$ LAEs from literature. This shows that it falls within the scatter of other similar LAEs, which may be interpreted as evidence as similar avenues of Lyα visibility. The Spearman correlation of both distributions are positive with very low P-values, indicating strong positive correlations.

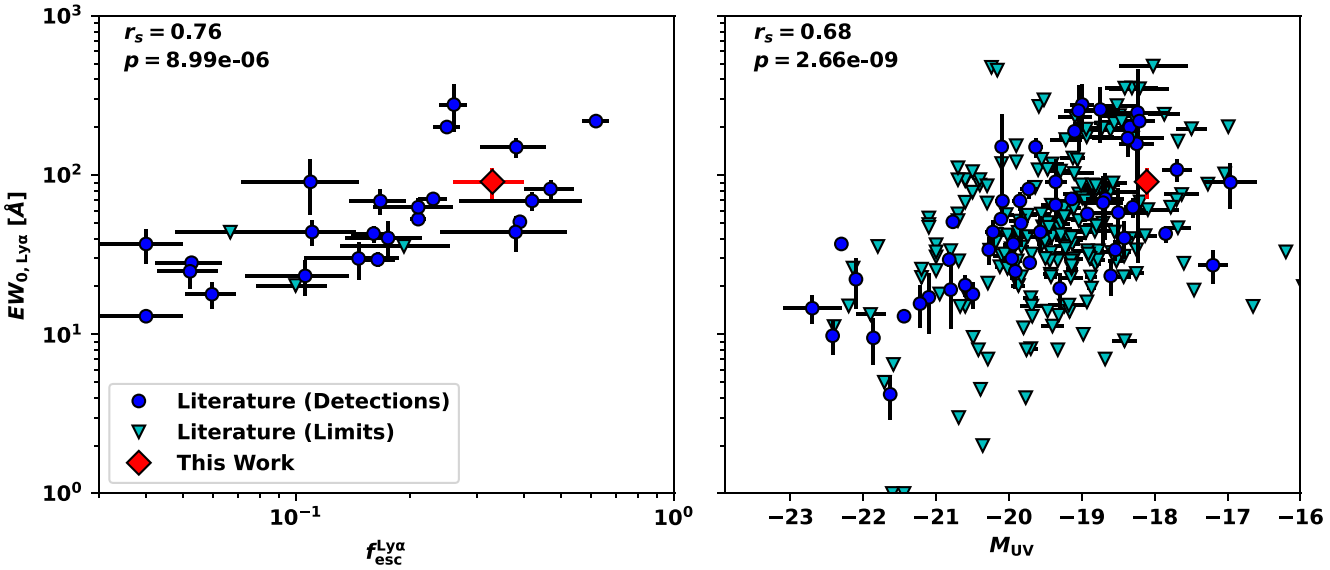

Figure E1. Placement of UNCOVER_20466 on distributions of $\mathrm{EW}_{0,\mathrm{Ly}\,\alpha}$ as a function of $f_{\rm esc}^{\mathrm{Ly}\,\alpha}$ (derived with fiducial ISM conditions; left panel) and $M_{\rm UV}$ (right panel), as shown by a red marker. For comparison, we plot the values of $z > 7$ galaxies from literature (E. Vanzella et al. 2011; Y. Ono et al. 2012; M. A. Schenker et al. 2012; M. Song et al. 2016; L. Pentericci et al. 2018; A. Hoag et al. 2019; S. Fuller et al. 2020; V. Tilvi et al. 2020; R. Endsley et al. 2022; I. Jung et al. 2022; M. Tang et al. 2023; L. Napolitano et al. 2024; M. Tang et al. 2024; Y. Kageura et al. 2025; C. J. Willott et al. 2025; G. C. Jones et al. 2025a. The value of $M_{\rm UV} = -18.11$ for UNCOVER_20466 is taken from S. Fujimoto et al. (2024). For each correlation, we present a Spearman coefficient (r_s) and p-value (p) for the detections.

This paper has been typeset from a TEX/LATEX file prepared by the author.